INORGANIC CHEMISTRY FRONTIERS

RESEARCH ARTICLE

View Article Online
View Journal

Cite this: DOI: 10.1039/d5qi01968k

Evidence for thermally activated delayed fluorescence in iridium(III) complexes

Piotr Pander, *[a,b] Dawid Nastula,[a] Paulina H. Marek-Urban, [a,b,c] Valery N. Kozhevnikov [d] and J. A. Gareth Williams [e]

In this work we report the second ever example of a fully experimentally confirmed thermally activated delayed fluorescence (TADF) in a dinuclear Ir(III) complex. The said complex displays a singlet–triplet gap ΔE_{ST} = 28 ± 5 meV, in agreement with the computational prediction of 31.1 meV – a value smaller than the previous TADF Ir(III) complex. We also demonstrate a proof-of-concept, solution-processed OLED featuring this complex as the luminescent dopant in the emissive layer, achieving external quantum efficiency of up to ~10% and maximum luminance of 18 000 cd m^{-2} – values significantly exceeding those reported earlier for Ir(III) TADF. These findings are preceded by a detailed consideration of spectral signs of TADF in the already known Ir(III) complexes. The spectral overlap of photoluminescence (PL) with strong (*i.e.*, spin-allowed) absorption bands is unusual for phosphorescent metal complexes, because the PL originates from the triplet state, which is normally significantly lower in energy than the lowest-lying singlet. In this study, we have scrutinized literature data on iridium(III) complexes that likewise show significant overlap between absorption and PL, and we conclude that a small singlet–triplet energy gap ΔE_{ST} in these complexes results in a TADF contribution to their emission. Such a mechanism has hitherto been overlooked in the large body of iridium(III) chemistry. We use computations to clarify the nature of the excited states in these complexes, demonstrating that the distinctive S_1 and T_1 character of states can be identified as well as confirming that ΔE_{ST} is small enough for TADF to occur at room temperature.

Received 25th September 2025,
Accepted 6th December 2025

DOI: 10.1039/d5qi01968k

rsc.li/frontiers-inorganic

1. Introduction

Iridium(III) complexes play a pivotal role in research and technology. They are used in a plethora of applications, from organic light-emitting diodes (OLEDs)[1–3] and light-emitting electrochemical cells (LEECs),[4–6] to bioimaging, phototherapy, photochemistry and photocatalysis.[7–9] The popularity of Ir(III) complexes in OLEDs remains somewhat uncontested, despite the low earth abundance of this metal and enthusiastic efforts to identify alternatives. Although they are widespread, have we really understood fully the excited-state properties of Ir(III) complexes? The d^6, pseudo-octahedral Ir(III) ion can induce a very strong heavy atom effect, facilitating the formally forbidden process of $T_1 \rightarrow S_0$ phosphorescence.[10] It is the resulting fast triplet radiative decay rates – and correspondingly high emission efficiency – that account for the popularity of Ir(III) complexes as luminescent dopants in OLEDs. Nevertheless, the ubiquity and apparent simplicity of this model means that other competing luminescent mechanisms may have been overlooked, yet they may also contribute to the overall photoluminescence (PL) decay of iridium(III) luminophores.

The process of thermally activated delayed fluorescence (TADF) was first identified decades ago (under the name E-type fluorescence) as a mechanism by which triplet excited states may lead to efficient emission, through $T_1 \rightarrow S_1$ (re-)population of the singlet state and subsequent $S_1 \rightarrow S_0$ radiative decay, as opposed to phosphorescence.[11] Recently, TADF emitters that function in this way have become one of the leading competitors to phosphorescent complexes in OLEDs and beyond.[12–14] Although now widely associated with purely organic systems, TADF is relatively common among various metal complexes such as those of the coinage metals Cu(I), Ag(I), and Au(I/III), which are widely investigated as blue OLED emitters.[15–19] TADF has also been identified in Pd(II),[20–22] Sn(IV),[23] and, more recently, certain Pt(II)[24–27] complexes.

At first glance, it may not be clear how TADF could benefit, or even apply, to luminophores that already have a strong

[a]Faculty of Chemistry, Silesian University of Technology, M. Strzody 9, 44-100 Gliwice, Poland. E-mail: piotr.pander@polsl.pl
[b]Centre for Organic and Nanohybrid Electronics, Silesian University of Technology, Konarskiego 22B, 44-100 Gliwice, Poland
[c]Faculty of Chemistry, Warsaw University of Technology, Noakowskiego 3, 00-664 Warsaw, Poland
[d]Department of Applied Sciences, Faculty of Health and Life Sciences, Northumbria University, Newcastle Upon Tyne, Tyne and Wear, NE1 8ST, UK
[e]Department of Chemistry, Durham University, South Road, Durham, DH1 3LE, UK

heavy atom effect, such as Ir(III) and Pt(II) complexes. However, it may still offer a significant advantage in accelerating the radiative decay of such luminophores: it supports the already relatively fast triplet radiative decay by providing an additional, even faster decay channel (Fig. 1).[25] Such TADF complexes are much less reliant on the spin–orbit coupling (SOC) originating from the heavy metal ion, which poses a challenging limitation for NIR (near-infrared) phosphors, for example.[24] In such cases, the need for π-extended aromatic ligands to obtain low-energy emissive states often limits the metal character of the excited state, hence slowing down the metal-facilitated $T_1 \rightarrow S_0$ radiative decay.[28] Meanwhile, the use of TADF complexes displaying faster radiative decay than their non-TADF counterparts may be beneficial for the overall operational stability of blue OLEDs, by ensuring that undesired excited-state degradation pathways have little time to compete with emission. Furthermore, even small contributions from higher energy excited states involved in TADF (*e.g.*, fluorescence from S_1) may provide purer blue PL, as the S_1 state is always at least a few tens of meV above the T_1.

A hallmark of the TADF mechanism in conventional emitters is typically the presence of strong charge-transfer (CT) states arising from a donor–acceptor molecular structure, which leads to low HOMO–LUMO absolute overlap, defined as $O = \int |\phi_i| |\phi_j| \mathrm{d}r$ (where i, j are the identifying numbers of the two orbitals considered)[29] and hence to a small ΔE_{ST}.[30] In the case of cyclometallated complexes, the metal ion and, often, some of the auxiliary ligands typically act as donors, and π-conjugated heterocyclic ligands as acceptors, giving rise to metal-to-ligand CT (= MLCT) states.[26,31] These states are, however, no different from non-metal CT states in the sense that they can also lead to reduced HOMO–LUMO overlap, just as in organic TADF emitters.[32]

The recent discovery by some of the current authors of an interplay between TADF and phosphorescence in a di-iridium (III) complex[31] has led us to re-examine other Ir(III) complexes in the existing literature that demonstrate similar properties. Our analysis – described in this paper – shows that TADF may, in fact, be contributing to the fast effective emission rates in many such cases. A range of Ir(III) complexes were identified and selected for study (Fig. 4), based on certain spectral features they display that are more characteristic of TADF rather than phosphorescence. We analyse their reported experimental absorption and PL spectra as well as radiative decay rate constants. We then probe the relevant electronic states of these complexes computationally. Our findings point to higher-lying excited states (*i.e.*, other than T_1) directly contributing to the radiative decay in many cases. Given the computational picture of these states having dominating singlet character, there is no doubt that TADF does contribute to the PL in at least some Ir(III) luminophores, but it has previously been overlooked. We believe that the discovery can profoundly modify the current understanding of this group of luminescent metal complexes.

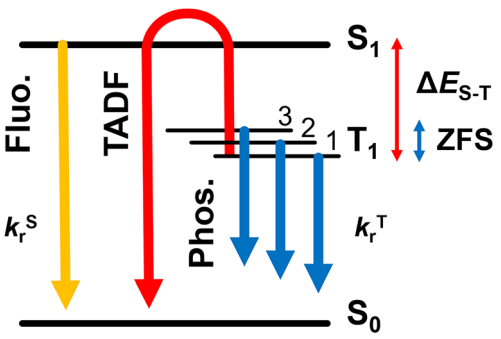

Fig. 1 Scheme illustrating the cooperative function of photoluminescence originated from T_1 sublevels (1, 2, 3) and the S_1 state when in thermal equilibrium with T_1 (TADF). The zero-field splitting (ZFS) is depicted as ΔE_{1-3}; ΔE_{ST} is the energy difference between T_1 and S_1; k_r^S and k_r^T are the radiative rate constants of S_1 and T_1 respectively.

2. Identifying signs of TADF emissions: significance of Stokes shifts and the Strickler–Berg approach

We first analyse the absorption–emission spectral overlap (henceforth referred to as "spectral overlap") of emitters of known luminescent nature, presented in Fig. 2. The model absorption and PL spectra of these luminophores can be found in Fig. 3. Fluorescent emitters typically display small Stokes shifts and pronounced spectral overlap, except where there is a significant reorganisation in the excited state.[33] We will simplify this discussion to include only emitters with small distortions between the ground and excited states. 9,10-Diphenylanthracene (**DPA**) and **fluorescein** are taken as examples of a fluorescent emitter: they display a clear mirror image between their respective absorption and emission bands, with the lowest absorption band in question being highlighted with a grey underlay. In transition metal phosphorescent emitters like the Pt(II) complex **Pt-Spiro**[34] and an Ir(III) complex **4-TCNIr**, weak $S_0 \rightarrow T_1$ absorption bands are discernible which overlap with the phosphorescence. For rigid, transition-metal TADF emitters, we would expect a spectral overlap more akin to **DPA** and **fluorescein**: see **Pt-TADF**[24] and other reported Pt(II) delayed fluorescence emitters.[25,26] Where the CT character of the MLCT transition is larger, the Stokes shift may be correspondingly larger, as in the reported **Ir-TADF** luminophore.[31] Some Cu(I) complexes are similar in this respect.[15]

We now attempt to draw quantitative conclusions from the above-mentioned spectral overlap by using the Strickler–Berg relationship.[35] In their original work, Strickler and Berg presented eqn (1):

$$\frac{1}{\tau_0} = 2.880 \times 10^{-9} n^2 \left\langle \tilde{\nu}_f^{-3} \right\rangle_{Av} \frac{g_l}{g_u} \int \varepsilon d \ln \tilde{\nu} \qquad (1)$$

where: τ_0 – natural decay lifetime of emission, s; n – refractive index of the medium; $\tilde{\nu}_f$ – average wavenumber of the PL spec-

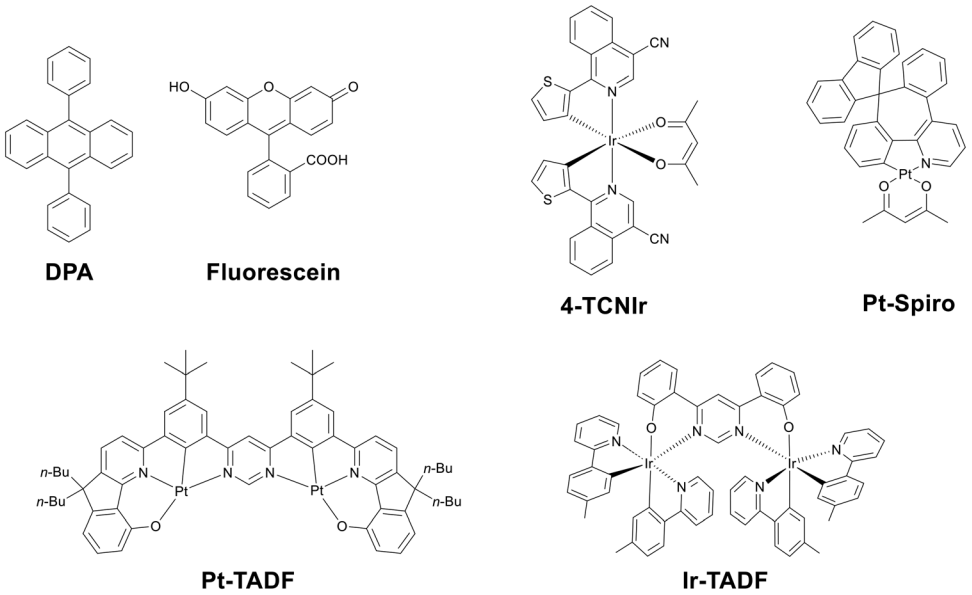

Fig. 2 Structures of exemplar fluorescent, phosphorescent, and TADF luminophores discussed in the text.

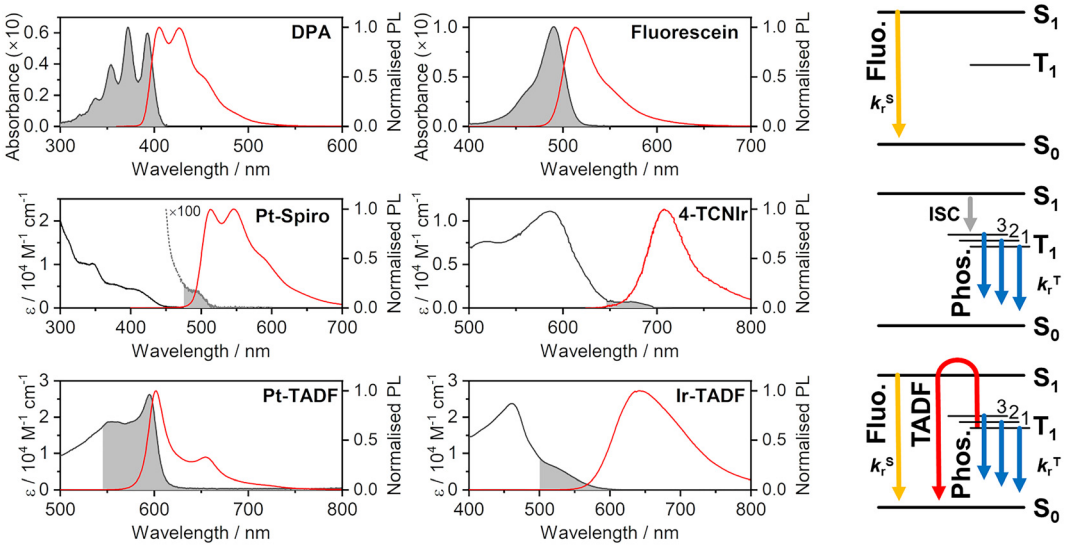

Fig. 3 Absorption and photoluminescence spectra of the luminophores shown in Fig. 2, in solution (c ~10^{-5} M) in: EtOH (**DPA**), 0.1 M NaOH (**fluorescein**), CH_2Cl_2 (**Pt-Spiro**, **TCNIr**), methylcyclohexane (**Pt-TADF**), and toluene (**Ir-TADF**). Areas shaded in grey indicate absorption bands considered in the Strickler–Berg approach.

trum, cm^{-1}; g_l – multiplicity of the lower state, so g_l = 1 for S_0; g_u – multiplicity of the upper state, so g_u = 1 or 3 for S_1 and T_1 respectively; ε – extinction coefficient of absorption, M^{-1} cm^{-1}; $\tilde{\nu}$ – wavenumber representing points of the lowest absorption band in the spectrum, cm^{-1}.

For the purpose of this work, eqn (1) is simplified following its fruitful use in this final form in previous works by some of the current authors,[31] giving eqn (2) and (3). The simplification replaces the term $\langle \tilde{\nu}_f^{-3} \rangle_{Av}$ with the PL maximum of the spectrum $\tilde{\nu}_{max}^{-3}$. These equations differ in the term $\frac{g_l}{g_u}$ where, for fluorescence (eqn (2)), $\frac{g_l}{g_u} = 1$, while for phosphorescence (eqn (3)), $\frac{g_l}{g_u} = \frac{1}{3}$.

$$^{SB}k_r^S = 2.880 \times 10^{-9} n^2 \tilde{\nu}_{max}^{-3} \int \varepsilon d \ln \tilde{\nu} \quad (2)$$

$$^{SB}k_r^T = 2.880 \times 10^{-9} n^2 \tilde{\nu}_{max}^{-3} \frac{1}{3} \int \varepsilon d \ln \tilde{\nu} \quad (3)$$

The use of eqn (2) and (3) is straightforward for presumed fluorescent and phosphorescent emitters, respectively. For pre-

sumed TADF emitters we will generally use the former but also apply the latter for comparison.

As fluorescent dyes such as **fluorescein** or **DPA** have been extensively studied by Strickler and Berg in their original work, we focus on phosphorescent and TADF emitters. Eqn (3) is used in order to calculate the ${}^{SB}k_r^T$ in each case, giving 3.5×10^4 s^{-1} for **Pt-Spiro** and 2.7×10^5 s^{-1} for **TCNIr** (the superscript SB will be used when referring to k_r values calculated in this way). These values are in good agreement with the reported k_r^T at RT of 6×10^4 s^{-1} and 4×10^5 s^{-1}, respectively. The small divergence between the SB-calculated and experimental values can be explained by experimental uncertainties and applied simplifications. The good agreement arises because the emissive transition is simply the transition from T_1 to S_0 with no other states involved. As demonstrated by Strickler and Berg, this is also expected for fluorescent emitters (*i.e.* $S_1 \rightarrow S_0$).

In the TADF case, the spectral overlap is similar to that for fluorescent dyes, with ${}^{SB}k_r^S = 5.9 \times 10^7$ s^{-1} for **Pt-TADF** and 1.7×10^7 s^{-1} for **Ir-TADF**.[24,31] Even if one initially assumed a phosphorescent nature of this emission and applied eqn (3), then ${}^{SB}k_r^T = 2.0 \times 10^7$ s^{-1} and 0.5×10^7 s^{-1}, respectively. Regardless of the equation used, the reported values at RT are 4.0×10^5 s^{-1} for **Pt-TADF** and 3.5×10^5 s^{-1} for **Ir-TADF**, which makes the values obtained directly from the Strickler–Berg relationship 1 to 2 orders of magnitude too high. To shed some light on this discrepancy we look at the k_r^S estimated by fitting the temperature-dependent behaviour of their luminescence decays.[24,31] In this case, experimental values of 1.5×10^7 s^{-1} for **Pt-TADF** and $0.8–1.2 \times 10^7$ s^{-1} for **Ir-TADF** were obtained, which are clearly in line with those obtained from the Strickler–Berg approach. The agreement of ${}^{SB}k_r^S$ with k_r^S is strongly indicative of TADF, and so is the effective k_r being orders of magnitude smaller.

Other previously reported Pt(II) TADF emitters display a similar relationship between the spectral overlap, the SB-calculated k_r^S, and their TADF properties.[24,25,36] To the best of our knowledge there exist no unequivocally phosphorescent transition metal complexes showing spectral overlap with a strong absorption band (*i.e.*, strong like a singlet absorption $S_0 \rightarrow S_1$), but only with a weak (*i.e.*, $S_0 \rightarrow T_1$) absorption.

In TADF the final luminescent state is the S_1 (Fig. 1). As $k_r^S \gg k_r^T$, it accelerates the total effective decay rate. The effective decay rate constant is a function of temperature and its magnitude is somewhere between k_r^S and k_r^T,(*i.e.* $k_r^S > k_r > k_r^T$), which is a direct consequence of the Boltzmann statistics determining the repopulation of S_1 from T_1. In other words, metal–organic TADF systems will display a k_r larger than their phosphorescent counterparts, but lower than the singlet decay rate constant, including that obtained from the Strickler–Berg relationship. This conjecture will form the core reasoning in what follows.

The aim of this work is to demonstrate that the spectral overlap involving strong absorption bands and the resultant mismatch between the measured effective k_r (smaller) and ${}^{SB}k_r^S$ (larger) values in Ir(III) complexes are indicative of TADF. As shown above, the simple overlap of the absorption and PL spectra carries crucial information about the luminescent nature of the emitter. Equipped with this basis, we move on to study this relationship in published luminescent Ir(III) complexes.

3. Using the Strickler–Berg approach to identify "hidden" TADF

The selection of molecules for the study was made by screening the available literature for signs of significant spectral overlap, as discussed above, while considering high quality of the photophysical data reported. The selected compounds thus come from a limited number of seven studies, identified by the first digit of the codes in Fig. 4 (*i.e.*, 1–7). This digit is followed by a hyphen after which appears either the code used in the original publication, or an alternative designation to ensure unequivocal identification in the present context.

Given the previously demonstrated[25] role of dinuclearity of platinum(II) complexes in promoting higher singlet oscillator strength f ($S_1 \rightarrow S_0$) and smaller ΔE_{ST}, it is unsurprising that most of the compounds presented in Fig. 4 are dinuclear as these are the very traits promoting TADF. We believe that dinuclear platinum(II) as well as iridium(III) complexes – as we demonstrate in this work – present visibly more identifiable signs of TADF than their mononuclear counterparts. Although mononuclear complexes are more popular and clearly more versatile, the focus on dinuclear complexes in this work reflects the very early stage of research on TADF in iridium(III) complexes, rather than any intrinsic requirement for a second metal centre. It seems inevitable that follow-up works will focus more on mono-Ir(III) complexes as the subject becomes widespread.

The first group comprises of complexes that take advantage of a ditopic bis-*NCN*-chelating ligand: **1-*rac*** and **1-*meso***,[37] related to the platinum(II) complexes for which TADF has already been demonstrated.[26] For **1-*rac*** complex, we selected one of the enantiomers shown in Fig. 2. Complex **5-5**[38] uses the same bis-*NCN*-chelating ligand as previously, but a tridentate *CNC* capping ligand. Complex **5-3** is a mononuclear analogue of **5-5** presented in the same work. Compounds **2-5**, **2-6**,[39] and **3-Ir$_2$I$_2$**[40] are structurally similar to complexes **6-A1** to **6-A5** and **6-B1** and **6-C1**.[41] These three groups of complexes feature a ditopic bis-*CN*-chelating ligand in conjunction with tridentate *NCN* ligands and monodentate halides X = Cl, I to complete the coordination sphere. Complex **2-5** is a mononuclear complex related to **2-6**. The halide proves to be crucial to the TADF properties of these complexes, as we demonstrate later in the text. Although the majority of complexes presented in this section are dinuclear, some were selected as mononuclear reference systems, such as **4-CNIr** and **4-TCNIr**[42] as well as **7-B1**, **7-B2**, and **7-B3**.[43] These mononuclear complexes still display some spectral overlap, but to a lower degree than the dinuclear complexes above (Fig. 5). Experimental photophysical characteristics of the Ir(III) complexes discussed in this work are summarised in Table S1. All experimental results used in this section were adopted from the respective refer-

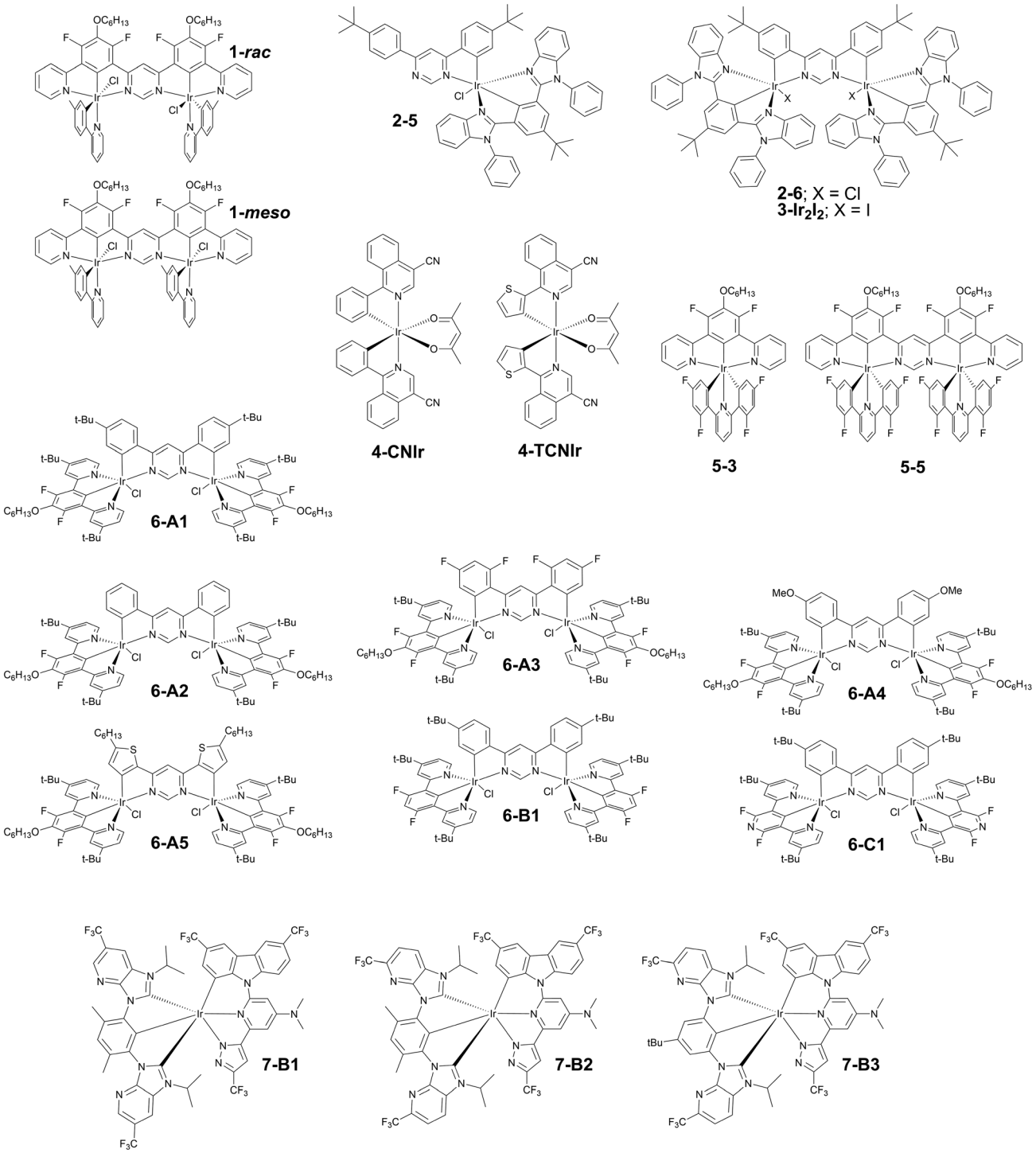

Fig. 4 Structures of the Ir(III) complexes used in the study.

ences: the reader should refer to the respective literature sources for experimental details.

We study the absorption and PL spectra of the complexes, presented in Fig. 4, in the same way as discussed in section 2 above. Considering the significant spectral overlap in most of the cases (Fig. 5), we use the SB method[35] to probe whether ${}^{SB}k_r$ values estimated from the absorption spectra correlate with the observed PL rate constants. The most rigorous approach would involve estimating the exact extent of the lowest-energy transition within the absorption spectrum, including the 0–0 as well as other vibronic bands. However, this approach is challenging given the unknown composition of the PL spectra, *i.e.*, presumably a mix of TADF and phosphorescence, as well as the mixed spin-multiplicity character

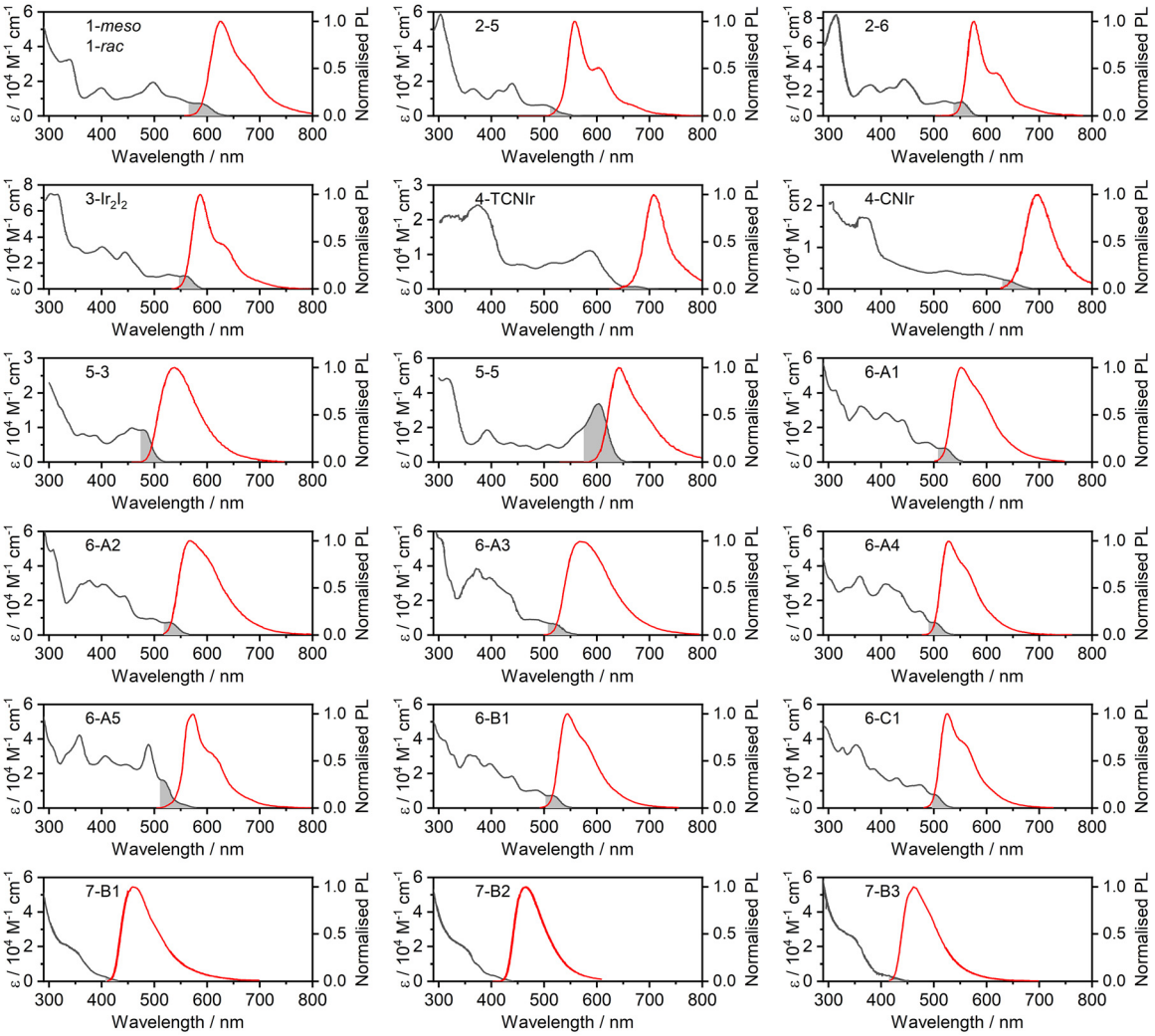

Fig. 5 Absorption (black lines) and photoluminescence (red lines) spectra of the studied iridium(III) complexes at room temperature, extracted from the respective original works.[38–40,42–45] The spectral regions shaded in grey represent the absorption bands taken into account for the calculations using the Strickler–Berg method.

of the absorption bands. Hence, we chose to only include the first vibronic band, acknowledging that this may lead to an underestimation in k_r calculated in this way. Similarly, PL λ_{max} values are used, due to the anticipated complexity of the experimental PL spectra, as discussed in section 2.[34,46] At this point, the constants ${}^{SB}k_r^S$ (eqn (2)) and ${}^{SB}k_r^T$ (eqn (3)) have no physical meaning before the main mode of photoluminescence: TADF or phosphorescence is identified. Once done, one of these values will become meaningless and hence ignored in the further discussion. We decided to include both of the said numerical values at this point to make our reasoning clearer. As explained earlier, we expect the ${}^{SB}k_r^T$ rate constants to roughly match the reported k_r for phosphorescent complexes. For these complexes the shaded absorption band is therefore assigned to the $S_0 \rightarrow T_1$ transition. The ${}^{SB}k_r^S$ is hence meaningless in this case and is ignored. In the case of a TADF complex the apparent constant ${}^{SB}k_r^T$ is expected to exceed the k_r as it is actually derived from a $S_0 \rightarrow S_1$ absorption band. In this case we identify the ${}^{SB}k_r^S$ as relevant in this case and ignore the other apparent constant ${}^{SB}k_r^T$. This reasoning is used for screening potential phosphorescent and TADF emitters in this work. Results comparing the reported k_r with either ${}^{SB}k_r^S$ and ${}^{SB}k_r^T$ calculated using the SB method are shown in Fig. 6 and presented in numerical form in the SI, Tables S1 and S2.

The results presented in Fig. 6 are arranged in the order of increasing ratio of ${}^{SB}k_r^T$ or ${}^{SB}k_r^S$ to the reported k_r. At first, one can clearly note that **4-CNIr** and **4-TCNIr** show good agreement between the reported k_r and calculated ${}^{SB}k_r^T$ values, and a ${}^{SB}k_r^T/k_r$ ~0.5–0.7, placing them as highly likely to be purely phosphorescent emitters with no contribution from TADF. A slight underestimation of the k_r^T in this case might originate from the inability to accurately assess the whole extent of the absorption band associated with the $S_0 \rightarrow T_1$ excitation. Another mono-Ir(III) complex **7-B2** also displays a rather good agreement, with ${}^{SB}k_r^T/k_r$ = 1.3. This is in line with our original

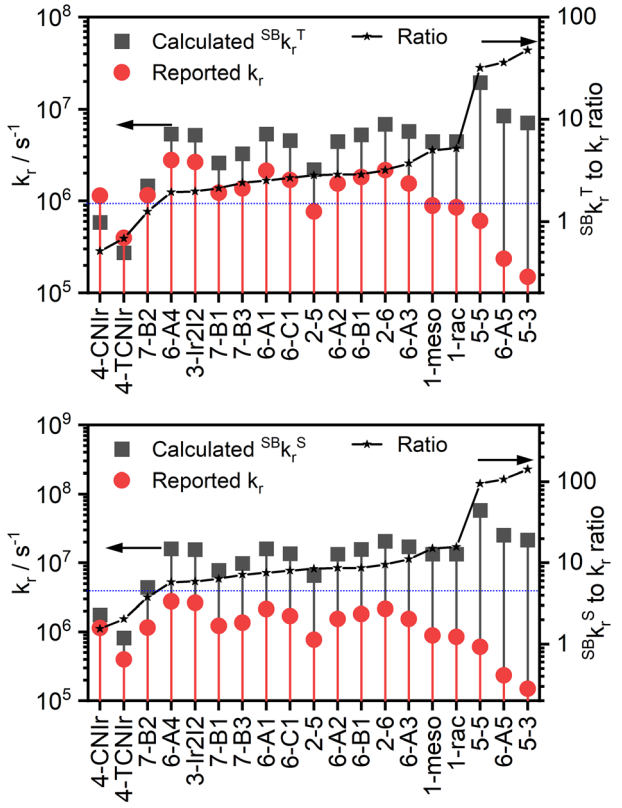

Fig. 6 Comparison of the apparent radiative rate constants $^{SB}k_r$ calculated using the Strickler–Berg method (dark grey squares) with those determined experimentally (red circles) – see Tables S1 and S2 for the associated numerical data. Note that these are numerical values obtained directly from the eqn (2) and (3) and they cannot be interpreted without context. The $^{SB}k_r^S$ are relevant only for TADF emitters, while $^{SB}k_r^T$ only for phosphorescent emitters. Refer to the article text for a detailed discussion on which of these values are relevant and which not.

hypothesis, namely that mononuclear complexes are generally less likely to show TADF and more likely to be purely phosphorescent. The next complex **6-A4** shows $^{SB}k_r^T/k_r$ ~2, which we believe might start being significant. We draw an imaginary threshold at $^{SB}k_r^T/k_r$ = 1.5 to distinguish clear metal–organic phosphors, below the threshold, and potential TADF emitters above it. The same trend can be obtained for the $^{SB}k_r^S/k_r$ ratio, but now the $^{SB}k_r^S$ is clearly not relevant for phosphorescent emitters (*i.e.*, there is no doubt that the analysed electronic transition is of $S_0 \rightarrow T_1$ character for them, hence the $^{SB}k_r^S$ is meaningless here).

The significance of the potential TADF behaviour becomes more apparent as the $^{SB}k_r^S/k_r$ ratio increases. This is because the stronger, presumably $S_0 \rightarrow S_1$ absorption band generates a larger $^{SB}k_r^S$, promoting the potential TADF behaviour, as explained earlier. The largest $^{SB}k_r^S/k_r$ ratio, at ~100, is found for three emitters: **5-3**, **5-5**, and **6-A5**. We will discuss these cases individually later, but at this point it is crucial to note that the original work presenting **5-3** and **5-5** identified them as showing a "TADF-*like*" behaviour.[38] In the light of the current state-of-the-art we believe that the behaviour is indeed TADF. Furthermore, a computational study[47] that incorporates spin–orbit coupling effects has demonstrated that the behaviour of **5-3** can indeed be explained with TADF, confirming the conclusions of the current work, as discussed later.

As we demonstrate in this section, the reported decay rate constants k_r in most of the presented iridium(III) complexes do not correlate with the values expected from the Strickler–Berg approach. This behaviour strongly indicates that in those cases the observed PL is not due to phosphorescence alone and that TADF is probably involved. This view is supported by earlier evidence of iridium(III) and platinum(II) complexes with TADF showing analogous behaviour to the ones discussed here.

4. Modelling TADF in transition metal complexes

The luminescent decay rate constants of transition metal complexes can generally be described with eqn (4), considering the radiative rate constants of the three principal triplet sublevels of T_1 – denoted 1, 2, and 3 – and the energy gaps between them:[10]

$$k_r^{1-3} = \frac{k_r^1 + k_r^2 e^{-\frac{\Delta E_{1,2}}{k_B T}} + k_r^3 e^{-\frac{\Delta E_{1,3}}{k_B T}}}{1 + e^{-\frac{\Delta E_{1,2}}{k_B T}} + e^{-\frac{\Delta E_{1,3}}{k_B T}}} \quad (4)$$

where k_r^{1-3} is the cumulative radiative decay rate constant of the phosphorescent complex at a given temperature T, s^{-1}; k_r^1, k_r^2, k_r^3 are radiative decay rate constants of the three T_1 sublevels, s^{-1}; $\Delta E_{1,2}$, $\Delta E_{1,3}$ is the energy gap between the states indicated in the subscript, eV; k_B is the Boltzmann constant, 8.617×10^{-5} eV K^{-1}; T is temperature, K. We assume that the states in question remain in an equilibrium.

When the S_1 state is thermally accessible, at RT for example, another term can be added, such as in eqn (5), where 4 denotes S_1 as the fourth state in consideration:[10,38]

$$k_r^{1-4} = \frac{k_r^1 + k_r^2 e^{-\frac{\Delta E_{1,2}}{k_B T}} + k_r^3 e^{-\frac{\Delta E_{1,3}}{k_B T}} + k_r^4 e^{-\frac{\Delta E_{1,4}}{k_B T}}}{1 + e^{-\frac{\Delta E_{1,2}}{k_B T}} + e^{-\frac{\Delta E_{1,3}}{k_B T}} + e^{-\frac{\Delta E_{1,4}}{k_B T}}} \quad (5)$$

Eqn (5) can also be presented as:

$$k_r^{1-4} = \frac{k_r^1 + k_r^2 e^{-\frac{\Delta E_{1,2}}{k_B T}} + k_r^3 e^{-\frac{\Delta E_{1,3}}{k_B T}} + k_r^S e^{-\frac{\Delta E_{ST}}{k_B T}}}{1 + e^{-\frac{\Delta E_{1,2}}{k_B T}} + e^{-\frac{\Delta E_{1,3}}{k_B T}} + e^{-\frac{\Delta E_{ST}}{k_B T}}} \quad (6)$$

In eqn (5) and (6), k_r^{1-4} is the cumulative decay rate constant considering phosphorescence and TADF from the S_1 state, s^{-1}; $\Delta E_{1,4}$ or ΔE_{ST} is the energy gap between the lowest T_1 sublevel and the S_1 state, eV; k_r^S – radiative decay rate constant of the S_1 state, s^{-1}.

In certain cases, especially when the experimental results to which the model is fitted lack data in certain temperature ranges like 1–20 K, the fit would be over-parametrised if using eqn (5) or (6). Thus, a simplified eqn (7) can be used, assuming that the T_1 sublevels 1 and 2 are virtually thermalised at the temperatures of the experiment, *i.e.* $e^{-\frac{\Delta E_{1,2}}{k_B T}} = 1$:

$$k_r^{1-4} = \frac{2k_r^{1,2} + k_r^3 e^{-\frac{\Delta E_{1,3}}{k_B T}} + k_r^S e^{-\frac{\Delta E_{ST}}{k_B T}}}{2 + e^{-\frac{\Delta E_{1,3}}{k_B T}} + e^{-\frac{\Delta E_{ST}}{k_B T}}} \quad (7)$$

For calculations of the percent contribution of TADF and phosphorescence, we consider the contribution of each term in the numerator to the sum of these terms:

$$\%\text{TADF} = 100\frac{k_r^S e^{-\frac{\Delta E_{ST}}{k_B T}}}{k_r^1 + k_r^2 e^{-\frac{\Delta E_{1,2}}{k_B T}} + k_r^3 e^{-\frac{\Delta E_{1,3}}{k_B T}} + k_r^S e^{-\frac{\Delta E_{ST}}{k_B T}}} \approx 100\frac{k_r^S e^{-\frac{\Delta E_{ST}}{k_B T}}}{2k_r^{1,2} + k_r^3 e^{-\frac{\Delta E_{1,3}}{k_B T}} + k_r^S e^{-\frac{\Delta E_{ST}}{k_B T}}} \quad (8)$$

$$\%\text{PHOS} = 100\frac{k_r^1 + k_r^2 e^{-\frac{\Delta E_{1,2}}{k_B T}} + k_r^3 e^{-\frac{\Delta E_{1,3}}{k_B T}}}{k_r^1 + k_r^2 e^{-\frac{\Delta E_{1,2}}{k_B T}} + k_r^3 e^{-\frac{\Delta E_{1,3}}{k_B T}} + k_r^S e^{-\frac{\Delta E_{ST}}{k_B T}}} \approx 100\frac{2k_r^{1,2} + k_r^3 e^{-\frac{\Delta E_{1,3}}{k_B T}}}{2k_r^{1,2} + k_r^3 e^{-\frac{\Delta E_{1,3}}{k_B T}} + k_r^S e^{-\frac{\Delta E_{ST}}{k_B T}}} \quad (9)$$

From the above equations, one can also obtain the above introduced parameters at $T \to \infty$ by assuming all Boltzmann terms are equal to 1. It can clearly be seen that even at $T \to \infty$ there is a limit to the decay lifetime and percent contribution of TADF and the latter mathematically never reaches 100%.

When calculating decay components computationally one may use a straightforward relationship between the oscillator strength f of a given transition and the radiative rate constant k_r:[48,49]

$$k_r = \frac{n^2 \nu^2 f}{1.5} \quad (10)$$

where n is the refractive index of the medium; ν is the wavenumber representing the electronic transition, cm^{-1}; f is the transition oscillator strength (also denoted as f_{osc} in other parts of the text).

In this work we obtain computational values of k_r^{1-3} and k_r^{1-4} using eqn (4) and (5), while variables k_r^1 to k_r^3 and k_r^S are determined directly from the computational ν and f using eqn (10).

5. Computational study

The computational study undertaken in this work is used to supplement the existing experimental results, presented in previous literature, rather than for making claims based solely on computation. For example, very thorough photophysical studies are often accompanied by simple TD-DFT calculations and lack computational approaches that include spin–orbit coupling and relativistic effects, such as in the methods used here. The approach used in our work allows not only to model singlet and triplet decay rates, but also to distinguish singlet from triplet states – a prerequisite of any TADF-inclusive model of electronic states. As we demonstrate below, these results merely confirm what is already evident from the experimental data and can be used to explain the mechanistic principles which are otherwise inaccessible.

We first consider the accuracy of the computational modelling. The methodology used in this work has already been successful and accurate in describing the previous example of a TADF iridium(III) complex **Ir-TADF**. The k_r^S, ΔE_{ST}, as well as the cumulative k_r^T have been estimated with sufficient accuracy to precisely reproduce the behaviour of the observed k_r with temperature. The same computational approach has also been used successfully to study dinuclear platinum(II) complexes displaying TADF[36] and accurately estimate the k_r^T of mononuclear platinum(II) luminophores, as in the case of **Pt-Spiro**.[34] As we demonstrate in this work, our computational approach is rather accurately predicting experimental variables relevant to TADF. What can be noted is that the very approach in question tends to overestimate the ΔE_{ST}, giving false negatives for TADF, but no true false positives were observed. It proves accurate in estimating the k_r^S of multiple dinuclear complexes, but fails for metal–iodide systems, *i.e.* M–I, giving significantly underestimated values.[26] This, however, is a rather known flaw of such DFT-based approaches to strong charge-transfer systems.[50]

In our work, we employ density functional theory (DFT) and time-dependent DFT (TD-DFT) calculations at the BP86/def2-TZVP level implemented in Orca[51,52] to generate the T_1 geometries (Fig. S7–S16). Single-point energy calculations used B3LYP/def2-TZVP level of theory with spin–orbit coupling, (ZORA),[53,54] *quasi*-degenerate perturbation theory (QDPT),[55,56] and CPCM for the appropriate solvent used in the experiments (listed in Table S1). In this case, ZORA-corrected def2-TZVP basis sets[57] were employed for all light atoms, and a segmented all-electron, relativistically-contracted (SARC) def2-TZVP basis set for Ir and I. These settings have previously been used to model an earlier example of a TADF di-Ir(III) complex,[31] with a good agreement between the computational model and experiment. All pertinent computational results are listed in Tables S3–S27 and shown in Fig. S1–S23. At this level of theory, we observe splitting of every T_n state into three *quasi*-degenerate sublevels as well as a significant S–T mixing, leading to contamination of triplet states with singlet admixtures and likewise singlet states with triplet admixtures.

We start from the general assessment of the molecular orbital landscape in the studied systems. The orbital iso-surfaces relevant to the S_1 and T_1 states are presented in Fig. 7 and 8 for **2-6**, **3-Ir$_2$I$_2$**, **6-A5**, and **6-B1**, and in Fig. S1–S6 for the remaining complexes. First of all, it may be noted that the presence of a transition metal ion, iridium(III) for example, creates sufficient spin–orbit coupling to relax the spin selection rules, allowing not only accelerated $T_1 \to S_0$ transition, but also intersystem crossing (ISC) as well as the reverse ISC (RISC) between S_1 and T_1 states directly, without the necessary participation of assistant states as is usually the case in metal-free TADF (Table S27).[58] That being said, we observe no particular state nature to be relevant to TADF in the discussed systems. What appears to be relevant are the numerical indicators, such as the three key constants describing TADF: k_r^S, ΔE_{ST} and k_r^T, and how orbital pairing affects them. The orbital nature of S_1 and T_1 states is summarised in Table S25, while

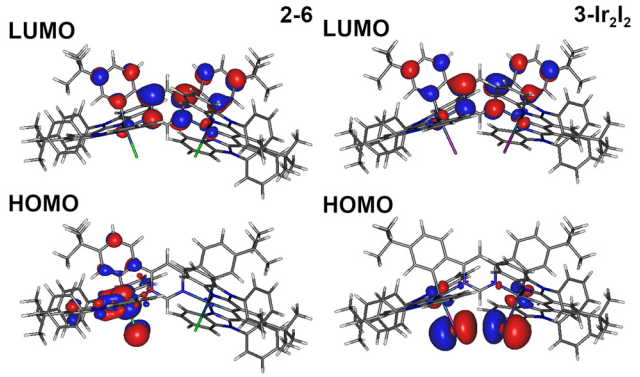

Fig. 7 Molecular orbitals involved in the S_1 and T_1 states in complexes **2-6** and **3-Ir$_2$I$_2$**. In both cases the S_1 and T_1 states can be described as a HOMO → LUMO transition.

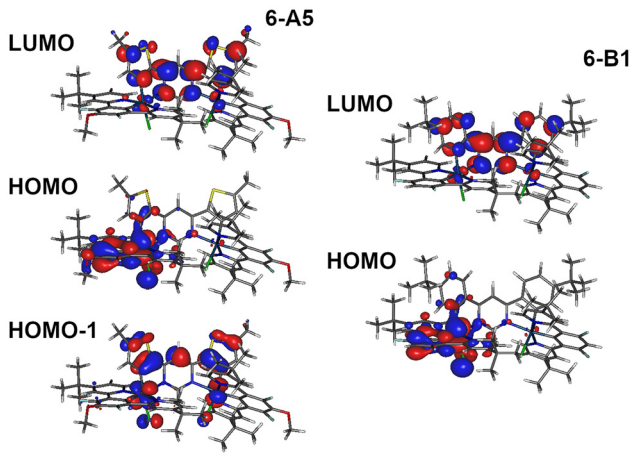

Fig. 8 Molecular orbitals involved in the S_1 and T_1 states in complexes **6-A5** and **6-B1**. In both cases, the S_1 can be described as a HOMO → LUMO transition. The T_1 in **6-B1**, like S_1, can be described as a HOMO → LUMO transition, but the T_1 in **6-A5** is of HOMO−1 → LUMO nature. MO pairing for other complexes can be found in the SI, Fig. S1–S6.

the pertinent spin–orbit coupling matrix elements $\langle T_1|\hat{H}_{SO}|S_1\rangle$ are collected in Table S27.

The nature of the S_1 and T_1 excited states spans from strongly CT, like MXLCT (metal-halogen-to-ligand charge-transfer) in complexes **2-6**, **3-Ir$_2$I$_2$**, **6-A1** to **6-A4**, **6-B1** and **6-C1**, to a mixed MLCT-LC (ligand-centred) in **5-3** and **5-5**. This distinction is visible in the experimental data through the stronger $S_0 \rightarrow S_1$ absorption, hence larger $f_{osc}(S_0 \rightarrow S_1)$ in the latter two. Therefore, the distinction between TADF and phosphorescence becomes more apparent for excited states with more LC admixture and likewise less apparent for stronger charge-transfer character of the excited state.

Our calculation returns SOC states which are the electronic states identifiable at the level of theory involving SOC and they are represented as a linear combination of TD-DFT states (*i.e.* S_n and T_n). The assessment of the nature of the electronic states is made by analysing the contributions of the T_1, S_1, and S_n TD-DFT states into each of the SOC states and the said contributions are collected in Tables S6–S24. The picture of the electronic excited states generally is very clear, with the T_1, T_2, and S_1 being easy to identify within SOC states 1 to 7 (the T_1 and T_2 states split into 3 SOC states each, therefore we are taking into consideration 3 + 3 + 1 = 7 SOC states). Example excited-state diagrams are presented in Fig. 9 for complexes **2-6**, **3-Ir$_2$I$_2$**, and **6-A1**, and in Fig. S17–S23 for the other complexes. In all cases SOC states 1–3 constitute the *quasi*-degenerate sublevels of T_1, while state 4 displays a substantial (albeit variable) singlet character. The remaining states 5–7 constitute the *quasi*-degenerate sublevels of T_2. In the exceptional cases of **4-TCNIr** and **6-A5**, S_1 character can be attributed to state 7 instead of 4, with T_2 constituting SOC states 4–6 instead of 5–7. The energy difference between SOC state 1 and the lowest singlet state is often of the order of 100 meV or significantly less, small enough for the S_1 state to be re-populated at RT and thus to be involved in the luminescent process. To improve our understanding of this behaviour and model the luminescence of our complexes as a function of temperature, the Boltzmann ratios between SOC state 1 and states 2–7 are calculated at 295 K (see Table S4 for Boltzmann coefficients). In most cases, the S_1 state is in equilibrium with the T_1 sublevels at RT, leading to a relevant singlet population, indicating that phosphorescence and TADF both contribute to the effective radiative decay rate constant at this temperature. This situation is, however, far from a pure TADF emission in iridium(III) complexes (although one would always expect trace contributions of phosphorescence according to the relative rate constants in a given case), but it demonstrates that the PL of these luminophores is a mixture of the two, comprising both singlet and triplet contributions.

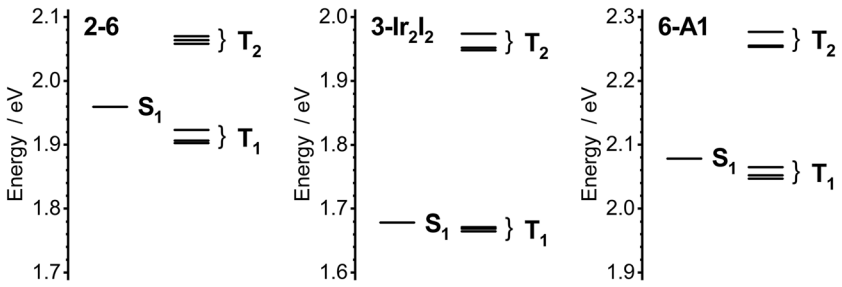

Fig. 9 Excited state energy diagram for complexes **2-6**, **3-Ir$_2$I$_2$** and **6-A1** showing vertical transition energies at T_1 geometry.

We first consider **2-6** and **3-Ir$_2$I$_2$** as they differ only in the identity of the monodentate halide ligand X = Cl or I. Their calculated ΔE_{ST} values are 57 and 14 meV respectively, consistent with a previously identified trend in related complexes that X = I leads to a smaller ΔE_{ST} compared to the X = Cl analogue.[26] This is due to the stronger electron-donating properties of I *versus* Cl affecting the electron-donor properties of the Ir–X moiety. Complexes incorporating an electron-rich halide ligand X display stronger electron-donor properties of the metal centre by introduction of the halide *p* electrons. These two complexes, along with **6-A1** to **6-A5**, **6-B1** and **6-C1**, represent a group showing MXLCT excited states, *i.e.*, those where the Ir–X (X = Cl, I) is the dominating donor moiety. In such cases, the electron-donating or -withdrawing character of the attached auxiliary halide ligand significantly modulates the electronic properties of the complex. The ZFS values are 20 and 7 meV for **2-6** and **3-Ir$_2$I$_2$**, respectively, while the calculated k_r^T is smaller in the latter. Clearly, the luminescence properties of **3-Ir$_2$I$_2$** reported in the original work[39] should be associated with the smaller ΔE_{ST}, and thus a more significant contribution of TADF. The contribution of halide *p* orbitals to the HOMO of both complexes (Fig. 7) does not significantly contribute to the overall heavy-atom effects, as these are dominated by the Ir(III) centre, as found in dinuclear complexes of the Pt(*NCN*)-X type.[26]

We now consider the case of complexes **5-3** and **5-5**, for which a *TADF-like* behaviour has previously been reported, by demonstrating that a fourth excited state is involved in the luminescence at RT.[38] Our computational analysis shows that one can determine the said 4th state (SOC state 4) to be of S_1 character. The ΔE_{ST} is smaller in **5-5** than in **5-3** which may be attributed to the presence of the strongly electron-deficient pyrimidine in the former. The presence of two Ir(III) centres linked with a common pyrimidine bridge may also be the cause for lower ΔE_{ST} and larger $f_{osc}(S_0 \rightarrow S_1)$ in **5-5** than in **5-3** – an effect which we are yet to fully understand. Although the ΔE_{ST} obtained from our calculations (Table S3) is visibly larger than the gap obtained experimentally, the other calculated characteristics clearly point to the S_1 and hence TADF being involved. Hence, we believe that this earlier example does, in fact, demonstrate a TADF mechanism, mediated through an excited state with a predominant S_1 character. We note that an earlier computational study conducted solely on **5-3** came to the same conclusion.[47]

Complexes **6-A1** to **6-A5**, as well as **6-B1** and **6-C1**, structurally resemble **2-6**. They are of the Ir–Cl type and display ΔE_{ST} < 70 meV, except for **6-A5** where $\Delta E_{ST} \approx 260$ meV. We ascribe the generally small ΔE_{ST} in this group of complexes to the presence of X = Cl and to the MXLCT nature of the excited S_1 and T_1 states, as detailed above. In **6-A5**, the phenyl-pyrimidine moieties are replaced by thienyl-pyrimidine groups which leads to the introduction of a low-energy T_1 state. The frontier molecular orbitals reveal that the new triplet state involves the thienyl groups and shows a different orbital pairing from that of S_1 (Fig. 8). From this behaviour of **6-A1** and that of the other complexes in the same work, one may conclude that the smallest ΔE_{ST} is attained for the S_1 and T_1 states with the same, rather than different, orbital pairing. The same is not usually considered optimal in the context of conventional metal-free TADF emitters as, there, the $\langle T_1|\hat{H}_{SO}|S_1\rangle \approx 0$ due to the near-identical orbital nature of the respective ^{3}CT and ^{1}CT states.[58–61] In this case a second triplet state must be involved to introduce sufficient SOC, allowing a fast pathway for ISC and RISC. However, in the context of iridium(III) complexes, the $\langle T_1|\hat{H}_{SO}|S_1\rangle$ is usually sufficient to allow direct RISC and ISC between the said states, without the necessity for other states being involved (Table S27).

Complexes **1-*rac*** and **1-*meso*** also contain the Ir–Cl moiety; $\Delta E_{ST} \approx 100$ meV is relatively high, while $f(S_1 \rightarrow S_0) \approx 0.01$ is limited, which results in only a relatively modest effect of TADF, at least from the computational standpoint. We aim to study this group of complexes in a follow-up work to gain some further insight.

Interestingly, the mononuclear complexes **7-B1** to **7-B3** display ΔE_{ST} that is sufficiently small for the S_1 excited state to be populated at RT, but the relatively insignificant singlet oscillator strength $f_{osc}(S_1 \rightarrow S_0)$ renders TADF of little effect in enhancing the effective radiative rate constant. This finding highlights the point raised in our earlier work,[25] namely that for heavy metal complexes, it is necessary for there to be not only a small ΔE_{ST} but also a substantial $f_{osc}(S_1 \rightarrow S_0)$ for TADF to be relevant.

To sum up this part of the section, we find that the coordination pattern of the complex has the most significant effect on parameters promoting TADF, while there is currently little evidence for any important effects of the particular substituents on the cyclometallating ligands. However, the introduction of thiophenes generally lowers the T_1 energy of the complex, increasing the ΔE_{ST}. Dinuclear *vs.* mononuclear design of the complex also offers a very different behaviour, with the TADF-facilitating properties being promoted in the former.

To test the reliability of our results and assumptions, we verify whether the calculated k_r^S values match the $^{SB}k_r^S$ figures. We expect them to match, as they should in principle represent the same physical quantity. The k_r^S obtained from the calculations do generally agree with the $^{SB}k_r^S$ values (Fig. 10). These matching results demonstrate that, overall, the assumptions made for calculating $^{SB}k_r^S$ are correct; *i.e.*, the studied absorption band in question is indeed associated with the $S_0 \rightarrow S_1$ excitation rather than something else. We believe that the k_r^S of **3-Ir$_2$I$_2$** is underestimated by the calculation due to the strong charge-transfer nature of the S_1 state. This issue is further discussed and resolved later in this section. In the case of **4-CNIr** and **4-TCNIr** the mismatch is directly related to these two variables – $^{SB}k_r^S$ and k_r^S – representing different physical quantities. In other words, the computed k_r^S is representative of the S_1 state, while the $^{SB}k_r^S$ is calculated from what is actually the $S_0 \rightarrow T_1$ absorption band (and hence has little physical meaning on its own). This agrees with the conclusions made solely from the Strickler–Berg analysis earlier in the text that the lowest absorption bands in complexes **4-CNIr** and **4-TCNIr** should

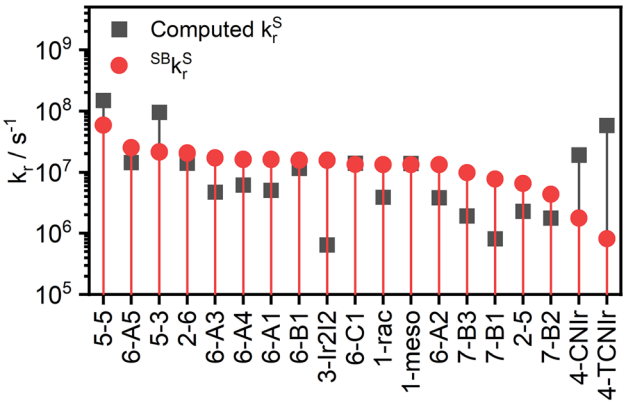

Fig. 10 Comparison of the singlet radiative decay rate constants $^{SB}k_r^S$ (dark grey squares) with the computed radiative decay rate constants k_r^S (red circles), shown on an exponential scale.

represent direct triplet absorption, demonstrating how the computational and Strickler–Berg approaches agree with each other.

We now model the decay rate constant k_r of the studied complexes using methodology described previously (Fig. 11 top).[31] Pertinent radiative decay rate constants and other parameters can be found in the SI, Tables S1–S5. For most of the cases, radiative rate constants solely reliant on phosphorescence decay are underestimated: the inclusion of TADF is necessary to account for the experimentally observed values. Complexes **6-A1** to **6-A5**, as well as **6-B1** and **6-C1**, show that our computational approach correctly predicts the effects of TADF on effective PL decay rate constants at RT. The calculations well match the experimental data as to the involvement of TADF: small ΔE_{ST} values are found for complexes **6-A1** to **6-A4**, **6-B1** and **6-C1**, which show fast radiative decay, while **6-A5** displays a large ΔE_{ST} such that TADF is minimal and the decay is slow. The potential effect of TADF on the k_r is less evident in **7-B1** to **7-B3** and in **1-*rac*** and **1-*meso*** due to the combination of a relatively small $f_{osc}(S_1 \rightarrow S_0)$ and a larger $\Delta E_{ST} \approx 100$ meV. In **5-3** and **5-5**, the ΔE_{ST} is likely to be overestimated, hence the calculated effects of TADF appear negligible. Perhaps most interesting is the comparison between **2-6** and **3-Ir_2I_2**, where the effect of TADF on k_r is evident in the former but negligible in the latter, with the computed k_r significantly underestimated with respect to the experimental value. In this case, the computation underestimates $f_{osc}(S_1 \rightarrow S_0)$ to be 2.4×10^{-3}, compared to $f_{osc}(S_1 \rightarrow S_0) = 0.036$ from the SB method. For comparison, the computed $f_{osc}(S_1 \rightarrow S_0) = 0.038$ for **2-6** is much closer to the SB-calculated $S_1 \rightarrow S_0$ value of 0.046.

We now replace the k_r^S obtained from the calculation with $^{SB}k_r^S$ and once again calculate the effective radiative rate constants k_r including TADF (Fig. 11 bottom). The results are similar overall to those using the k_r^S obtained from computations. We focus on the examples of **2-6** and **3-Ir_2I_2**, for which the computation accurately predicts the k_r in the former but not the latter. The prediction of k_r becomes accurate for both complexes once the $^{SB}k_r^S$ is introduced instead of k_r^S obtained

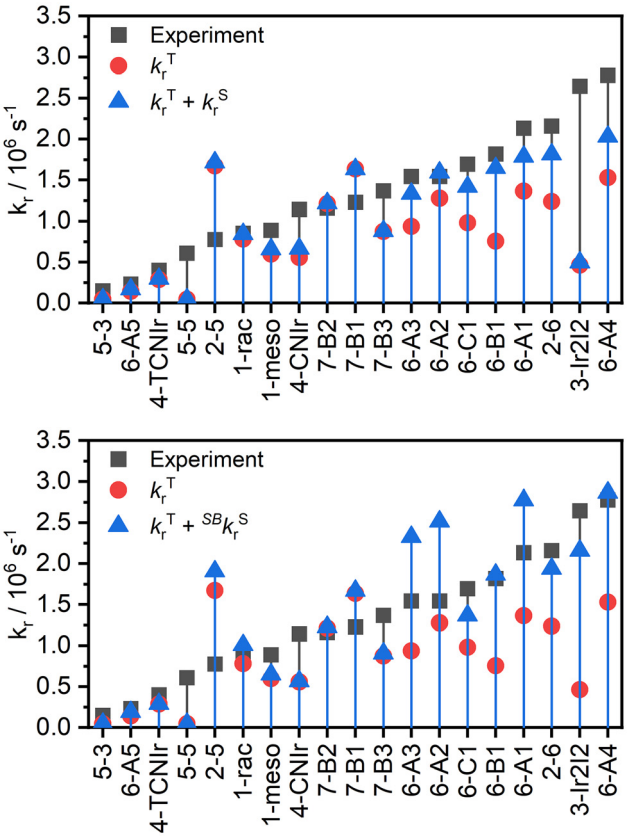

Fig. 11 Comparison of calculated radiative rate constants at 295 K with the experimental radiative decay rate constants (dark grey squares): phosphorescence only (red circles); phosphorescence + TADF (blue triangles). Top: All decay rates obtained computationally; bottom: $^{SB}k_r^S$ obtained from the Strickler–Berg ($S_1 \rightarrow S_0$) method.

from computations. This demonstrates a weakness of the computational approach related to the underestimation of the $f_{osc}(S_1 \rightarrow S_0)$ for strong MXLCT states. It also offers a simple solution, as the said value may be obtained more accurately experimentally using the Strickler–Berg approach. Overall, the modelled k_r values for all complexes are in a rough agreement with the experiment, while an excellent match can be claimed for a handful of complexes. We believe this to be a very good result overall as calculation of the k_r requires seven computed parameters and it is hard to expect that all of them will give a perfect match for every complex.

Finally, we use the example of the complex **6-B1** to model the expected behaviour of the PL lifetime as a function of temperature T, with and without TADF. Fig. 12 top shows the decay lifetime τ as a function of T in these two scenarios. This relationship demonstrates that changes in τ at $T > 50$ K can be ascribed both to the thermal equilibrium between the *quasi*-degenerate T_1 sublevels and to TADF, due to a relatively small $\Delta E_{ST} = 42.2$ meV and the ZFS being only slightly smaller at 30 meV. TADF gradually grows in significance with increasing T, with the onset at ~50 K, reaching a 50% contribution at ~200 K and 58% at 295 K (Fig. 12 bottom). TADF is the most

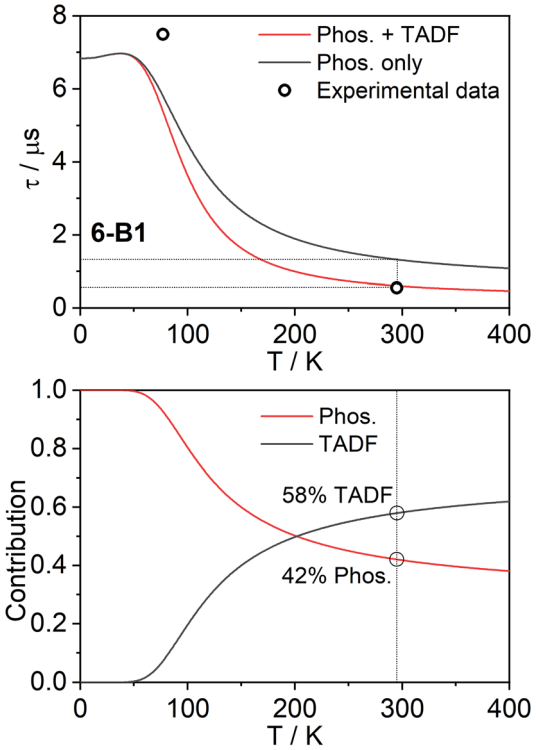

Fig. 12 Top: Comparison of the modelled variation of the PL lifetime of complex **6-B1** with temperature, considering phosphorescence only (black line) and phosphorescence together with the TADF mechanism (red line). Black circles indicate experimental data points. Bottom: Relative contributions of phosphorescence and TADF as function of temperature. The values highlighted in the figure refer to T = 295 K. Note that the uncertainty on the experimental data points was not determined in the original study.[41]

significant component of the emission, but phosphorescence is nevertheless present. This picture is fully consistent with the behaviour demonstrated in the earlier account of TADF in Ir(III) complexes,[31] but the onset of TADF appears at lower temperatures due to the relatively small ΔE_{ST}.

6. TADF in 6-A1

We selected complex **6-A1** as the most suitable candidate to experimentally demonstrate TADF behaviour as it is representative of structurally related complexes of the 6-series as well as **3-Ir$_2$I$_2$** and **2-6**. Complex **6-A1** was obtained as described previously.[45] Due to the small Stokes shift and the resultant spectral overlap, the best conditions to study TADF complexes are when using dilute polymer films. The complex was studied in thin polystyrene films at a concentration of 0.2% w/w. Steady state absorption and PL spectra of **6-A1** are presented in Fig. 13. The spectra recorded in toluene and polystyrene are similar, with the former being slightly red shifted with respect to the latter. The ϕ_{PL} = 0.57 in toluene, while a similar value of ϕ_{PL} = 0.56 has been recorded in polystyrene. We recorded steady-state PL spectra as a function of T using a narrow wave-

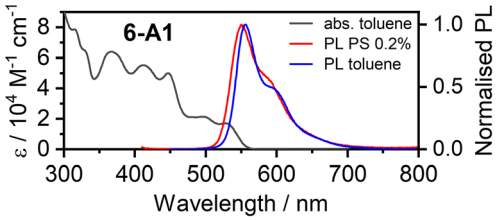

Fig. 13 Absorption and PL spectra of **6-A1** in toluene (c = 10^{-5} M) and polystyrene (0.2% w/w).

length range, allowing for improved spectral resolution, see Fig. 14 left. The PL spectra present the typical temperature-dependent behaviour seen in previous TADF complexes.[31,36] They gradually shift from one spectral shape, seen at higher temperatures and associated with TADF-dominated PL, to the other one, seen at lower temperatures and associated with phosphorescence. The spectra remain virtually invariant in the 90–295 K temperature range, while a faint rigidochromic blue shift can be observed upon cooling (see Fig. 15 right). This rigidochromic shift[62] has been observed previously and it may pose a significant obstacle in studies of TADF of both platinum(II) and iridium(III) complexes, as it potentially inhibits the direct measurement of ΔE_{ST}. The most significant spectral changes can be observed over the range 20 < T < 90 K, indicating that no significant TADF occurs at 20 K. The very subtle spectral change to both the onset and the two vibronic maxima suggests that TADF likely dominates the PL at T > 90 K and the spectral features observable in **6-A1** at RT are associated with the emission originating from S_1. Photoluminescence decay of **6-A1** in polystyrene remains monoexponential at all studied temperatures. The pertinent decay traces are collected in Fig. 15 left.

From the PL spectra onsets of **6-A1** (Fig. 14 left) we calculate ΔE_{ST} = 31 ± 5 meV. Fitting of the decay lifetimes using eqn (7) gives a similar value ΔE_{ST} = 28 ± 5 meV, and ZFS = 16 ± 1 meV (129 ± 8 cm^{-1}) and k_r^S = (2.0 ± 0.3) × 10^7 s^{-1}. These values are in a good agreement with the computational results presented earlier, *i.e.* ZFS = 17.8 meV and ΔE_{ST} = 31.1 meV, confirming the accuracy of our computational approach at least to this complex and perhaps to the other complexes of the **6**-series. The calculated k_r^S = 5.06 × 10^6 s^{-1} is slightly underestimated, but generally in line with the experimental data. The SB-calculated rate constant $^{SB}k_r^S$ = 1.6 × 10^7 s^{-1} is in an excellent agreement with the experimental k_r^S value. These results confirm the reliability of both our computational and SB-based approaches in determining certain constants describing the luminescent decay of **6-A1**. Given the close similarity between **6-A1** and other complexes of the **6**-series, except for **6-A5**, one can clearly conclude that all share the same principal characteristics as the former.

Complex **6-A1** displays a roughly two-fold reduction in its radiative decay lifetime due to TADF, as shown in Fig. 16 left. This is a similar magnitude to that reported earlier for **Ir-TADF**[31] and expected from the computations. The contri-

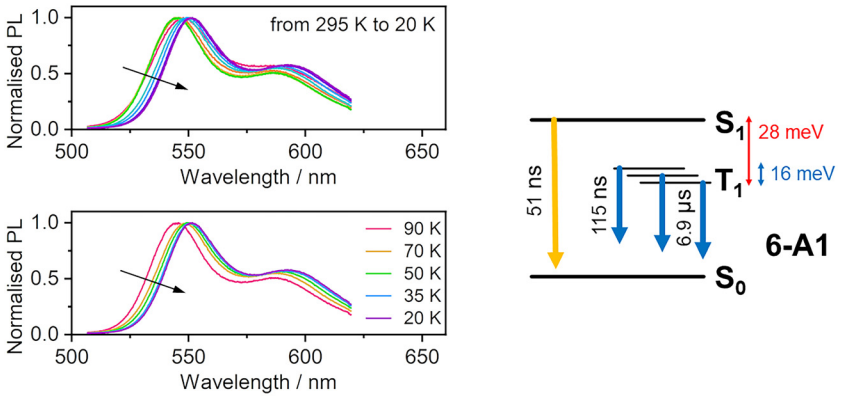

Fig. 14 Left: Normalised steady-state PL spectra recorded with 100 ns delay and 20 µs integration time. Top: All spectra recorded in the temperature range from 20 to 295 K; bottom: spectra recorded at temperatures from 20 to 90 K, highlighting the spectral change due to TADF quenching. Right: Schematic of the electronic excited states and radiative lifetimes in **6-A1**.

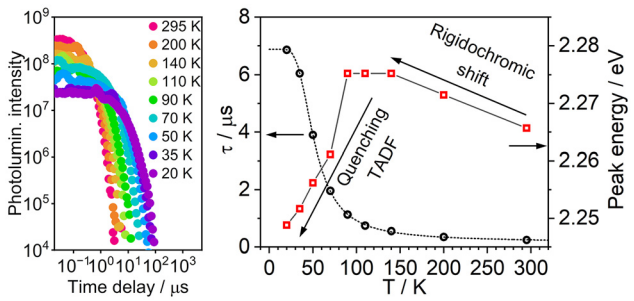

Fig. 15 Variable temperature study of photoluminescence in **6-A1**. Left: Photoluminescence decay traces recorded at temperatures indicated in figure legend; right: PL lifetimes and PL peak position as a function of temperature. Dotted line indicates the best fit according to eqn (7).

bution of TADF to the PL of **6-A1** is ~60% at 295 K (Fig. 16 right). The role of TADF in this group of luminophores is correlated with a shortening of the PL lifetime by a factor of 2 or more in comparison to the purely phosphorescent mechanism, but perhaps not more than by an order of magnitude. This highlights the importance of TADF in cases where the metal character is low, such as in NIR-emitting complexes that rely on π-extended ligands. Nevertheless, it becomes clear that the emission of some, if not many, iridium(III) complexes is significantly affected by TADF and it proves incorrect to consider their properties without evaluating the possible thermal population of singlet states.

7. Identification of other TADF emitters using reported experimental data

We study the reported temperature dependence of PL lifetime for some of the complexes discussed above – **2-6**, **3-Ir$_2$I$_2$**, **5-3**, and **5-5** – to identify whether there is any evidence for the suspected TADF behaviour (Fig. 17 and 18). The luminescence decay of **2-6** and **3-Ir$_2$I$_2$** can be explained with two models which give similar fit, but they involve a different number of variables. The model including three (Fit 1, eqn (7)) or two (Fit 2, eqn (11)) luminescent states can describe the experimental data very well, but we prefer the former. It gives two lifetime components that can be attributed to the two T_1 sublevels and a fast (<50 ns) component attributed to S_1 emission.

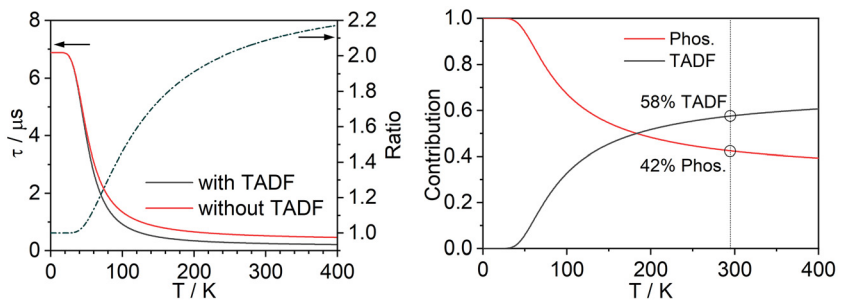

Fig. 16 Left: Line of best fit according to eqn (7) from Fig. 15 right (dark grey line) and the same fit but with the terms in eqn (7) associated with emission from the singlet state deleted (red line). The black dashed line is the ratio between the red and the dark grey lines, highlighting the significance of the TADF mechanism for the luminescent decay lifetime at T > 50 K. Right: Phosphorescence and TADF contributions calculated using eqn (8) and (9) with the vertical line indicating T = 295 K.

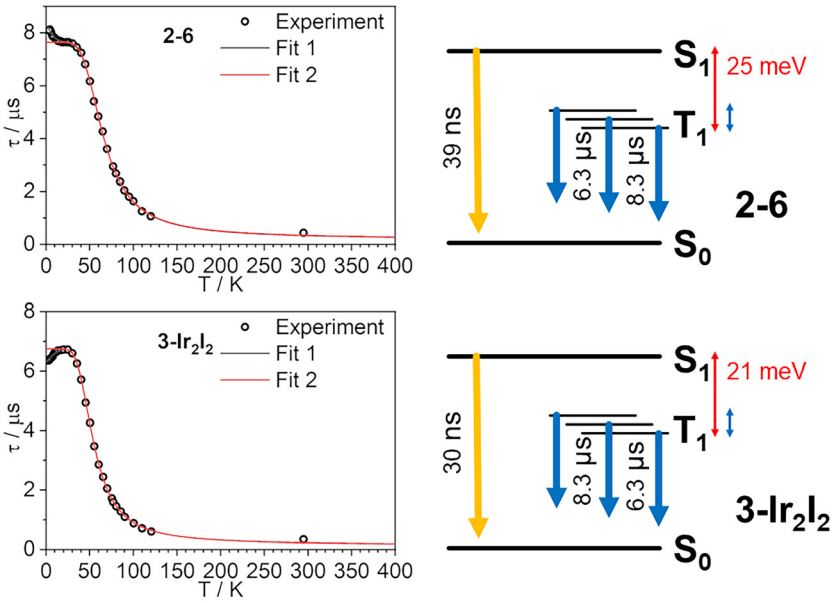

Fig. 17 Left: Photoluminescence decay lifetimes of **2-6** and **3-Ir$_2$I$_2$** reconstructed from the original work[40] (black circles) and fits obtained using eqn (7) and (11) (continuous grey and red lines); right: experimental model of luminescent electronic states of **2-6** and **3-Ir$_2$I$_2$**.

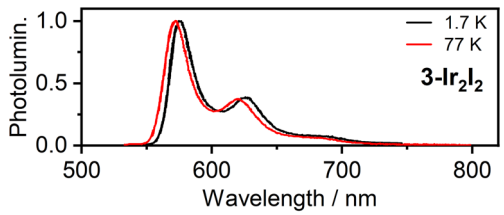

Fig. 18 Photoluminescence spectra of **3-Ir$_2$I$_2$** at 1.7 K and 77 K as reported in the original work.[40]

Considering the relative energy and radiative decay rate constant of this last state, it is clearly the singlet state predicted through the computational approach presented above and not a triplet state. Finding the fastest, third component attributed to the remaining T_1 sublevel is not possible due to the lack of data points at $T > 120$ K. We expect this component to display a lifetime of ~100 ns, in line with calculations and the behaviour of **6-A1**, analogous to **2-6** and **3-Ir$_2$I$_2$**. From these fits we obtain ΔE_{ST} values of 25 meV and 21 meV for **2-6** and **3-Ir$_2$I$_2$**, respectively.

$$k_r^{1-4} = \frac{3k_r^{1,2,3} + k_r^S e^{-\frac{\Delta E_{ST}}{k_B T}}}{3 + e^{-\frac{\Delta E_{ST}}{k_B T}}} \quad (11)$$

Furthermore, the original work featuring the **3-Ir$_2$I$_2$** complex displays PL spectra at 77 K as well as at 1.7 K. The behaviour observed in Fig. 18, where the PL at 1.7 K is red shifted to that at 77 K, resembles that observed in **6-A1**, Fig. 14, and can thus be interpreted in the same way. Based on our assessment of the photophysical properties of this complex and their similarity to **6-A1** we are certain that the PL spectrum at 77 K is most likely dominated by TADF (as occurs at 90 K for **6-A1**) and thus the spectrum at 1.7 K is associated with phosphorescence. The optical energy gap between the onsets of the two spectra is 24 ± 8 meV, which is in a good agreement with the experimental result obtained with eqn (7) (ΔE_{ST} = 21.1 ± 0.2 meV) as well as the computed ΔE_{ST} = 14.0 meV for this complex. The energy gap between the two lowest T_1 sublevels in **3-Ir$_2$I$_2$** is only ~1 meV, hence clearly not interfering with the observed ΔE_{ST} value discussed above.

For **5-3** and **5-5** the authors of the original work have reported emission contributions from states higher than T_1 (Fig. 19). This has later been computationally demonstrated to be TADF by Gao and Cui for **5-3**.[47] The behaviour of both complexes involving TADF is in line with our computational predictions, which demonstrate an unequivocal S_1 state above the three T_1 sublevels. Fitting of the data up to 120 K for **5-3** and **5-5** allows identification of the three decay components of the split T_1 sublevels (Fit 1, eqn (4)). Addition of the term describing the S_1 contribution accounts for the further shortening of the decay lifetime at RT to τ = 6.67 μs in **5-3** – a value projected assuming ϕ_{PL} = 1 – and τ = 1.31 μs in **5-5** (Fit 2, eqn (5)). Fit 2 is more of a guess than a proper fit. In this case we fix all variables at their values from Fit 1 except for τ^S, which is obtained from the SB approach above, and ΔE_{ST} – the only new variable we obtain from this guess. Nevertheless, the obtained ΔE_{ST} values are in line with the expected figures in this case, at 125 meV for **5-3** and 102 meV for **5-5**.

The summary of the model experimental parameters obtained in this section is presented in Table 1, alongside computational predictions. One may note that the computational k_r^S values roughly agree with the experimental data, except maybe for **3-Ir$_2$I$_2$**, as explained before. A better match

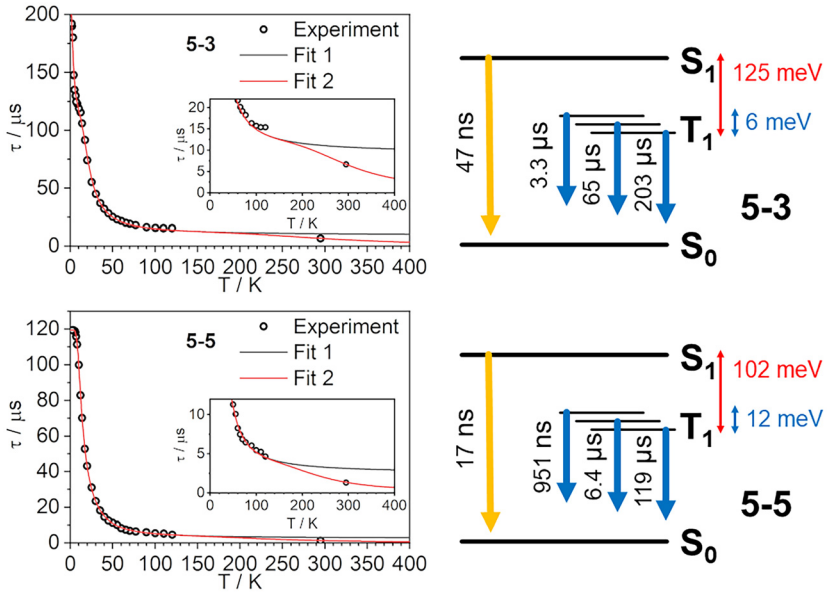

Fig. 19 Left: Photoluminescence decay lifetimes of **5-3** and **5-5** reconstructed from the original work[38] (black circles) and fits obtained using eqn (4) and (5) (continuous grey and red lines); right: experimental model of luminescent electronic states of **5-3** and **5-5**.

Table 1 Comparison between experimental constants and computational predictions for the five iridium(III) complexes discussed in this section

	6-A1		**2-6**		**3-Ir_2I_2**		**5-3**		**5-5**	
	Calc.	Exp.	Calc.	Exp.	Calc.	Exp.	Calc.	Exp.	Calc.	Exp.
k_r^S, 10^6 s^{-1} [a]	5.1	20 ± 3	14.2	22 ± 1	0.6	33 ± 1	95.8	21[e]	149.3	58[e]
ΔE_{1-3} (ZFS), meV[b]	17.8	16 ± 1	20.4	—[d]	6.8	—[d]	2.6	6.6 ± 0.3	4.8	12.3 ± 0.5
ΔE_{ST}, meV[c]	31.1	28 ± 5	56.8	24.7 ± 0.3	14.0	21.1 ± 0.2	380.9	125 ± 33	278.3	102 ± 14

[a] Singlet radiative decay rate constant. [b] Zero-field splitting. [c] S_1–T_1 energy gap. [d] Not obtained from the model. [e] Value assumed from the SB methodology.

can generally be obtained from the experimental SB values $^{SB}k_r^S$ at 16×10^6 s^{-1}, 21×10^6 s^{-1}, and 16×10^6 s^{-1} for **6-A1**, **2-6**, and **3-Ir_2I_2**, respectively (Table S2). The computational ΔE_{ST} values do not directly match the experiment, but a clear trend may be found (Fig. 20). The relationship between the experimental (y) and computational ΔE_{ST} (x), both values in meV, can be described by the equation $y = 0.29x + 15$. These types of linear relationships are common between experimental and computational data obtained using TD-DFT methods.[63] The meaning of the a and b in the $y = ax + b$ relationship depends on the intricate settings of the functional and basis set used and they have no physical meaning. However, we expect this approach to be useful for estimating computational ΔE_{ST} values of iridium(III) emitters studied in the future.

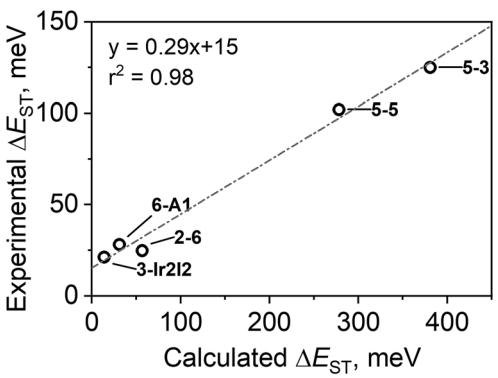

Fig. 20 Relationship between the calculated and experimental ΔE_{ST}.

8. OLED devices with 6-A1

TADF iridium(III) complex **6-A1** was tested as a luminescent dopant in solution-processed OLEDs. The architectures feature those successfully applied in a di-platinum(II) TADF complex reported earlier.[36] As **6-A1** displays a pronounced concentration quenching in the solid state, we employed doping concentrations of 1 and 3% w/w in two different OLED structures:

ITO | AI4083 (30 nm) | PVKH (10 nm) | mCP:PO-T2T (70 : 30) co. **6-A1** (1 or 3%) (~30 nm) | PO-T2T (50 nm) | LiF (0.8 nm) | Al (100 nm) – Device 1 (3%) and Device 2 (1%); ITO

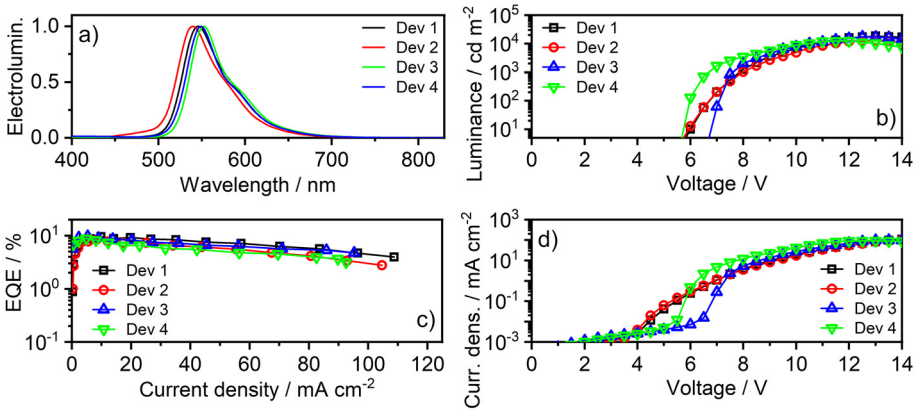

Fig. 21 Characteristics of electroluminescent devices using **6-A1** in the emissive layer: (a) EL spectra; (b) luminance *vs*. applied voltage; (c) external quantum efficiency (EQE) *vs*. current density; (d) current density *vs*. applied voltage.

| AI4083 (30 nm) | PVKH (10 nm) | mCP:PBD (60 : 40) co. **6-A1** (1 or 3%) (~30 nm) | TmPyPB (50 nm) | LiF (0.8 nm) | Al (100 nm) – Device 3 (3%) and Device 4 (1%).

The acronyms used to describe OLED architectures are defined in the Experimental section in the SI. The results are displayed in Fig. 21 and S24 and summarized numerically in Table S29 in the SI.

The OLEDs display behaviour akin to the similar structures used before, with the V_{ON} = 5.5–7 V at 10 cd m^{-2} and maximum luminance of up to 17 000–18 000 cd m^{-2} in Devices 1 and 3. Devices 2 and 4 display slightly lower maximum luminance at ~13 000 cd m^{-2}. OLEDs 1 and 3 (3% loading) display maximum EQE at ~10%, while 2 and 4 (1% loading) give slightly lower values of ~8–9%. This general behaviour can be explained by the emitter being unable to efficiently trap charge carriers at 1% loading, leading to some recombination occurring at the host molecules, and hence to energy losses. This is evident in Device 2 where a shoulder at 450–500 nm is associated with emission of the exciplex host mCP : PO-T2T. Electroluminescence spectra of Devices 1–4 are similar to the PL spectra in film or solution but display some variability that can be explained, on the one hand, with slightly different host polarity between mCP : PO-T2T and mCP : PBD (1 *vs*. 3 and 2 *vs*. 4) and, on the other, with small Stokes shift and the resultant PL self-absorption (1 *vs*. 2 and 3 *vs*. 4). A pronounced self-absorption in solution PL is common to other TADF platinum(II) or iridium(III) complexes while it is not generally observed for phosphorescent analogues.

9. Conclusions

It is clear that the overall understanding of the electronic excited states of iridium(III) complexes has not been complete. We as researchers have been misled by the simplicity of the three-state triplet-only model, which does not take singlet states into account, and by an *a priori* assumption that one cannot distinguish singlet and triplet states in *all* of these luminescent complexes. We therefore demonstrate a new and more complete model for studying luminescent iridium(III) complexes that necessarily includes S_1 states and TADF. Have we been wrong all along then? It does indeed appear that the failure to include TADF when considering the PL properties of iridium(III) complexes may lead to significant shortcomings in the analysis, leading to a danger of misinterpreting the behaviour. It may also lead to underestimation of their radiative decay rate when using computational modelling.

We have used computational methods to screen through a selection of Ir(III) complexes, identifying one of them as a potential candidate for an experimental study. The calculations accurately predict the electronic properties of complex **6-A1**, and we have proceeded to use this material as an exemplar luminescent dopant in OLEDs. With ΔE_{ST} = 28 ± 5 meV, and hence significant TADF, it displays excellent behaviour in solution-processed OLEDs, with maximum EQE and luminance values of ~10% and ~18 000 cd m^{-2}, respectively.

In conclusion, we have demonstrated that many Ir(III) complexes may emit through TADF, and provided a methodology for an easy identification of potential Ir(III) TADF emitters using only the most basic photophysical data. Our results confirm the hypothesis that TADF contributes to the PL in most of the studied iridium(III) complexes. In this work we have demonstrated that some established iridium(III) complexes display TADF, by using both new and earlier experimental results and computational modelling. We believe that recognising iridium(III) complexes as potential TADF emitters constitutes a significant breakthrough in understanding this group of transition metal compounds. As their use is widespread among many research fields, our findings will have a significant impact where the nature of the emitting state – singlet or triplet – is particularly important, such as in OLED applications.[43,64,65] The principal molecular design leading to TADF relies on an architecture where the metal centre acts as a donor, while the heteroaromatic ligands act as acceptors. In this respect the strongly electron-accepting pyrimidine is clearly an important component of a TADF Ir(III) complex. It

appears that dinuclear designs somewhat favour TADF or at least make it easier to be observed. Nevertheless, there remain many unknowns in the structure–property relationships governing TADF in iridium(III) complexes.

Conflicts of interest

There are no conflicts of interest to declare.

Data availability

Our supporting research data is available from Zenodo: **https://zenodo.org/doi/10.5281/zenodo.13692226**.

Supplementary information (SI) is available: details on data processing, computations and detailed explanations of the mathematical equations used, as well as supplementary data and figures. See DOI: **https://doi.org/10.1039/d5qi01968k**.

Acknowledgements

P. P. thanks the National Science Centre, Poland for funding, grant no. 2022/45/B/ST4/02689. This work made use of the facilities of the Hamilton HPC Service of Durham University. P. P. thanks Professor Andrew P. Monkman and Professor Fernando B. Dias for providing access to the experimental setups at Department of Physics at Durham University.

References

1 H. Yersin, Triplet Emitters for OLED Application. Mechanisms of Exciton Trapping and Control of Emission Properties, *Top. Curr. Chem.*, 2004, 1–26.
2 L. F. Gildea and J. A. G. Williams, in *Organic Light-Emitting Diodes (OLEDs)*, Elsevier, 2013, pp. 77–113.
3 J. M. Ha, S. H. Hur, A. Pathak, J.-E. Jeong and H. Y. Woo, Recent advances in organic luminescent materials with narrowband emission, *NPG Asia Mater.*, 2021, **13**, 53.
4 J. Zhang, L. Zhou, H. A. Al-Attar, K. Shao, L. Wang, D. Zhu, Z. Su, M. R. Bryce and A. P. Monkman, Efficient Light-Emitting Electrochemical Cells (LECs) Based on Ionic Iridium(III) Complexes with 1,3,4-Oxadiazole Ligands, *Adv. Funct. Mater.*, 2013, **23**, 4667–4677.
5 S. B. Meier, D. Tordera, A. Pertegás, C. Roldán-Carmona, E. Ortí and H. J. Bolink, Light-emitting electrochemical cells: recent progress and future prospects, *Mater. Today*, 2014, **17**, 217–223.
6 Y. Lin, C. Lu and H. Su, Long-Wavelength Light-Emitting Electrochemical Cells: Materials and Device Engineering, *Chem. – Eur. J.*, 2023, **29**(10), e202202985.
7 K. Teegardin, J. I. Day, J. Chan and J. Weaver, Advances in Photocatalysis: A Microreview of Visible Light Mediated Ruthenium and Iridium Catalyzed Organic Transformations, *Org. Process Res. Dev.*, 2016, **20**, 1156–1163.
8 J. C. Bawden, P. S. Francis, S. DiLuzio, D. J. Hayne, E. H. Doeven, J. Truong, R. Alexander, L. C. Henderson, D. E. Gómez, M. Massi, B. I. Armstrong, F. A. Draper, S. Bernhard and T. U. Connell, Reinterpreting the Fate of Iridium(III) Photocatalysts–Screening a Combinatorial Library to Explore Light-Driven Side-Reactions, *J. Am. Chem. Soc.*, 2022, **144**, 11189–11202.
9 H. Shi, R. C. Marchi and P. J. Sadler, Advances in the Design of Photoactivatable Metallodrugs: Excited State Metallomics, *Angew. Chem., Int. Ed.*, 2025, **64**(9), e202423335.
10 H. Yersin, A. F. Rausch, R. Czerwieniec, T. Hofbeck and T. Fischer, *The triplet state of organo-transition metal compounds. Triplet harvesting and singlet harvesting for efficient OLEDs*, Elsevier B.V., 2011, preprint, DOI: DOI: **10.1016/j.ccr.2011.01.042**.
11 C. A. Parker and C. G. Hatchard, Triplet-singlet emission in fluid solutions. Phosphorescence of eosin, *Trans. Faraday Soc.*, 1961, **57**, 1894.
12 H. Uoyama, K. Goushi, K. Shizu, H. Nomura and C. Adachi, Highly efficient organic light-emitting diodes from delayed fluorescence, *Nature*, 2012, **492**, 234–238.
13 Y. Tao, K. Yuan, T. Chen, P. Xu, H. Li, R. Chen, C. Zheng, L. Zhang and W. Huang, Thermally Activated Delayed Fluorescence Materials Towards the Breakthrough of Organoelectronics, *Adv. Mater.*, 2014, **26**, 7931–7958.
14 F. Fang, L. Zhu, M. Li, Y. Song, M. Sun, D. Zhao and J. Zhang, Thermally Activated Delayed Fluorescence Material: An Emerging Class of Metal-Free Luminophores for Biomedical Applications, *Adv. Sci.*, 2021, **8**, 2102970.
15 A. S. Romanov, L. Yang, S. T. E. Jones, D. Di, O. J. Morley, B. H. Drummond, A. P. M. Reponen, M. Linnolahti, D. Credgington and M. Bochmann, Dendritic Carbene Metal Carbazole Complexes as Photoemitters for Fully Solution-Processed OLEDs, *Chem. Mater.*, 2019, **31**, 3613–3623.
16 R. Czerwieniec, J. Yu and H. Yersin, Blue-Light Emission of Cu(I) Complexes and Singlet Harvesting, *Inorg. Chem.*, 2011, **50**, 8293–8301.
17 R. Czerwieniec and H. Yersin, Diversity of copper(I) complexes showing thermally activated delayed fluorescence: Basic photophysical analysis, *Inorg. Chem.*, 2015, **54**, 4322–4327.
18 A. S. Romanov, S. T. E. Jones, L. Yang, P. J. Conaghan, D. Di, M. Linnolahti, D. Credgington and M. Bochmann, Mononuclear Silver Complexes for Efficient Solution and Vacuum-Processed OLEDs, *Adv. Opt. Mater.*, 2018, **6**, 1801347.
19 D. Di, A. S. Romanov, L. Yang, J. M. Richter, J. P. H. Rivett, S. Jones, T. H. Thomas, M. A. Jalebi, R. H. Friend, M. Linnolahti, M. Bochmann and D. Credgington, High-performance light-emitting diodes based on carbene-metal-amides, *Science*, 2017, **356**, 159–163.
20 Z. Q. Zhu, C. Do Park, K. Klimes and J. Li, Highly Efficient Blue OLEDs Based on Metal-Assisted Delayed Fluorescence Pd(II) Complexes, *Adv. Opt. Mater.*, 2019, **7**, 1801518.

21 G. Li, Q. Chen, J. Zheng, Q. Wang, F. Zhan, W. Lou, Y. F. Yang and Y. She, Metal-Assisted Delayed Fluorescent Pd(II) Complexes and Phosphorescent Pt(II) Complex Based on [1,2,4]Triazolo[4,3- A[pyridine-Containing Ligands: Synthesis, Characterization, Electrochemistry, Photophysical Studies, and Application, *Inorg. Chem.*, 2019, **58**, 14349–14360.

22 P. W. Zach, S. A. Freunberger, I. Klimant and S. M. Borisov, Electron-Deficient Near-Infrared Pt(II) and Pd(II) Benzoporphyrins with Dual Phosphorescence and Unusually Efficient Thermally Activated Delayed Fluorescence: First Demonstration of Simultaneous Oxygen and Temperature Sensing with a Single Emitter, *ACS Appl. Mater. Interfaces*, 2017, **9**, 38008–38023.

23 A. Endo, M. Ogasawara, A. Takahashi, D. Yokoyama, Y. Kato and C. Adachi, Thermally Activated Delayed Fluorescence from Sn4+-Porphyrin Complexes and Their Application to Organic Light Emitting Diodes - A Novel Mechanism for Electroluminescence, *Adv. Mater.*, 2009, **21**, 4802–4806.

24 P. Pander, R. Daniels, A. V. Zaytsev, A. Horn, A. Sil, T. J. Penfold, J. A. G. Williams, V. N. Kozhevnikov and F. B. Dias, Exceptionally fast radiative decay of a dinuclear platinum complex through thermally activated delayed fluorescence, *Chem. Sci.*, 2021, **12**, 6172–6180.

25 P. Pander, A. V. Zaytsev, A. Sil, J. A. G. Williams, P.-H. Lanoe, V. N. Kozhevnikov and F. B. Dias, The role of dinuclearity in promoting thermally activated delayed fluorescence (TADF) in cyclometallated, N^C^N-coordinated platinum(II) complexes, *J. Mater. Chem. C*, 2021, **9**, 10276–10287.

26 P. Pander, A. V. Zaytsev, A. Sil, J. A. G. Williams, V. N. Kozhevnikov and F. B. Dias, Enhancement of thermally activated delayed fluorescence properties by substitution of ancillary halogen in a multiple resonance-like diplatinum(II) complex, *J. Mater. Chem. C*, 2022, **10**, 4851–4860.

27 A. Russegger, S. M. Fischer, A. C. Debruyne, H. Wiltsche, A. D. Boese, R. I. Dmitriev and S. M. Borisov, Tunable Self-Referenced Molecular Thermometers via Manipulation of Dual Emission in Platinum(II) Pyridinedipyrrolide Complexes, *ACS Appl. Mater. Interfaces*, 2024, **16**, 11930–11943.

28 D. N. Kozhevnikov, V. N. Kozhevnikov, M. Z. Shafikov, A. M. Prokhorov, D. W. Bruce and J. A. G. Williams, Phosphorescence vs Fluorescence in Cyclometalated Platinum(II) and Iridium(III) Complexes of (Oligo)thienylpyridines, *Inorg. Chem.*, 2011, **50**, 3804–3815.

29 T. J. Penfold, On Predicting the Excited-State Properties of Thermally Activated Delayed Fluorescence Emitters, *J. Phys. Chem. C*, 2015, **119**, 13535–13544.

30 T.-L. Wu, S.-H. Lo, Y.-C. Chang, M.-J. Huang and C.-H. Cheng, Steric Switching for Thermally Activated Delayed Fluorescence by Controlling the Dihedral Angles between Donor and Acceptor in Organoboron Emitters, *ACS Appl. Mater. Interfaces*, 2019, **11**, 10768–10776.

31 P. Pander, A. V. Zaytsev, A. Sil, G. V. Baryshnikov, F. Siddique, J. A. G. Williams, F. B. Dias and V. N. Kozhevnikov, Thermally activated delayed fluorescence in a deep red dinuclear iridium(III) complex: a hidden mechanism for short luminescence lifetimes, *Chem. Sci.*, 2023, **14**, 13934–13943.

32 F. B. Dias, Kinetics of thermal-assisted delayed fluorescence in blue organic emitters with large singlet–triplet energy gap, *Philos. Trans. R. Soc., A*, 2015, **373**, 20140447.

33 T. Hatakeyama, K. Shiren, K. Nakajima, S. Nomura, S. Nakatsuka, K. Kinoshita, J. Ni, Y. Ono and T. Ikuta, Ultrapure Blue Thermally Activated Delayed Fluorescence Molecules: Efficient HOMO-LUMO Separation by the Multiple Resonance Effect, *Adv. Mater.*, 2016, **28**, 2777–2781.

34 P. Pander, A. V. Zaytsev, L. G. Franca, F. B. Dias and V. N. Kozhevnikov, Unusual Excimer/Dimer Behavior of a Highly Soluble C,N Platinum(II) Complex with a Spiro-Fluorene Motif, *Inorg. Chem.*, 2023, **62**, 18465–18473.

35 S. J. Strickler and R. A. Berg, Relationship between Absorption Intensity and Fluorescence Lifetime of Molecules, *J. Chem. Phys.*, 1962, **37**, 814–822.

36 P. Pander, Y. M. Dikova, E. V. Puttock and J. A. G. Williams, Dinuclear platinum(II) complexes emitting through TADF: new ligand design to minimise aggregation and the S_1–T_1 energy gap, *Inorg. Chem. Front.*, 2024, **11**, 7545–7551.

37 P.-H. Lanoë, C. M. Tong, R. W. Harrington, M. R. Probert, W. Clegg, J. A. G. Williams and V. N. Kozhevnikov, Ditopic bis-terdentate cyclometallating ligands and their highly luminescent dinuclear iridium(III) complexes, *Chem. Commun.*, 2014, **50**, 6831–6834.

38 M. Z. Shafikov, R. Martinscroft, C. Hodgson, A. Hayer, A. Auch and V. N. Kozhevnikov, Non-Stereogenic Dinuclear Ir(III) Complex with a Molecular Rack Design to Afford Efficient Thermally Enhanced Red Emission, *Inorg. Chem.*, 2021, **60**, 1780–1789.

39 M. Z. Shafikov, R. Daniels and V. N. Kozhevnikov, Unusually Fast Phosphorescence from Ir(III) Complexes via Dinuclear Molecular Design, *J. Phys. Chem. Lett.*, 2019, **10**, 7015–7024.

40 M. Z. Shafikov, A. V. Zaytsev and V. N. Kozhevnikov, Halide-Enhanced Spin–Orbit Coupling and the Phosphorescence Rate in Ir(III) Complexes, *Inorg. Chem.*, 2021, **60**, 642–650.

41 R. E. Daniels, S. Culham, M. Hunter, M. C. Durrant, M. R. Probert, W. Clegg, J. A. G. Williams and V. N. Kozhevnikov, When two are better than one: bright phosphorescence from non-stereogenic dinuclear iridium (III) complexes, *Dalton Trans.*, 2016, **45**, 6949–6962.

42 Z. Chen, H. Zhang, D. Wen, W. Wu, Q. Zeng, S. Chen and W.-Y. Wong, A simple and efficient approach toward deep-red to near-infrared-emitting iridium(III) complexes for organic light-emitting diodes with external quantum efficiencies of over 10%, *Chem. Sci.*, 2020, **11**, 2342–2349.

43 Z.-L. Zhu, P. Gnanasekaran, J. Yan, Z. Zheng, C.-S. Lee, Y. Chi and X. Zhou, Efficient Blue Electrophosphorescence

and Hyperphosphorescence Generated by Bis-tridentate Iridium(III) Complexes, *Inorg. Chem.*, 2022, **61**, 8898–8908.

44 P.-H. Lanoë, C. M. Tong, R. W. Harrington, M. R. Probert, W. Clegg, J. A. G. Williams and V. N. Kozhevnikov, Ditopic bis-terdentate cyclometallating ligands and their highly luminescent dinuclear iridium(III) complexes, *Chem. Commun.*, 2014, **50**, 6831–6834.

45 R. E. Daniels, S. Culham, M. Hunter, M. C. Durrant, M. R. Probert, W. Clegg, J. A. G. Williams and V. N. Kozhevnikov, When two are better than one: bright phosphorescence from non-stereogenic dinuclear iridium (III) complexes, *Dalton Trans.*, 2016, **45**, 6949–6962.

46 M. Urban, P. H. Marek-Urban, K. Durka, S. Luliński, P. Pander and A. P. Monkman, TADF Invariant of Host Polarity and Ultralong Fluorescence Lifetimes in a Donor-Acceptor Emitter Featuring a Hybrid Sulfone-Triarylboron Acceptor, *Angew. Chem., Int. Ed.*, 2023, **62**, e202217530.

47 L.-Y. Peng, Z.-W. Li, G.-N. Pan, W.-K. Chen, Y.-J. Gao and G. Cui, Thermally activated delayed fluorescence of a Ir(III) complex: absorption and emission properties, nonradiative rates, and mechanism, *Phys. Chem. Chem. Phys.*, 2023, **25**, 6454–6460.

48 K. Mori, T. P. M. Goumans, E. van Lenthe and F. Wang, Predicting phosphorescent lifetimes and zero-field splitting of organometallic complexes with time-dependent density functional theory including spin–orbit coupling, *Phys. Chem. Chem. Phys.*, 2014, **16**, 14523–14530.

49 K. Nozaki, Theoretical Studies on Photophysical Properties and Mechanism of Phosphorescence in [fac -Ir(2-phenylpyridine) 3], *J. Chin. Chem. Soc.*, 2006, **53**, 101–112.

50 W. Zeng, S. Gong, C. Zhong and C. Yang, Prediction of Oscillator Strength and Transition Dipole Moments with the Nuclear Ensemble Approach for Thermally Activated Delayed Fluorescence Emitters, *J. Phys. Chem. C*, 2019, **123**, 10081–10086.

51 F. Neese, The ORCA program system, *Wiley Interdiscip. Rev.: Comput. Mol. Sci.*, 2012, **2**, 73–78.

52 F. Neese, Software update: The ORCA program system—Version 5.0, *Wiley Interdiscip. Rev.: Comput. Mol. Sci.*, 2022, **12**, e1606.

53 E. van Lenthe, E. J. Baerends and J. G. Snijders, Relativistic regular two-component Hamiltonians, *J. Chem. Phys.*, 1993, **99**, 4597–4610.

54 E. van Lenthe, E. J. Baerends and J. G. Snijders, Relativistic total energy using regular approximations, *J. Chem. Phys.*, 1994, **101**, 9783–9792.

55 M. Roemelt, D. Maganas, S. DeBeer and F. Neese, A combined DFT and restricted open-shell configuration interaction method including spin-orbit coupling: Application to transition metal L-edge X-ray absorption spectroscopy, *J. Chem. Phys.*, 2013, **138**, 204101.

56 B. de Souza, G. Farias, F. Neese and R. Izsák, Predicting Phosphorescence Rates of Light Organic Molecules Using Time-Dependent Density Functional Theory and the Path Integral Approach to Dynamics, *J. Chem. Theory Comput.*, 2019, **15**, 1896–1904.

57 F. Weigend and R. Ahlrichs, Balanced basis sets of split valence, triple zeta valence and quadruple zeta valence quality for H to Rn: Design and assessment of accuracy, *Phys. Chem. Chem. Phys.*, 2005, **7**, 3297.

58 F. B. Dias, J. Santos, D. R. Graves, P. Data, R. S. Nobuyasu, M. A. Fox, A. S. Batsanov, T. Palmeira, M. N. Berberan-Santos, M. R. Bryce and A. P. Monkman, The Role of Local Triplet Excited States and D-A Relative Orientation in Thermally Activated Delayed Fluorescence: Photophysics and Devices, *Adv. Sci.*, 2016, **3**, 1600080.

59 M. Chapran, I. Sahalianov, N. N. Karaush-Karmazin, G. Wiosna-Salyga, I. Glowacki, B. Luszczynska, P. Pander and G. V. Baryshnikov, Electronic Structure of Exciplexes and the Role of Local Triplet States on Efficiency of Thermally Activated Delayed Fluorescence, *ACS Appl. Electron. Mater.*, 2023, **5**, 1489–1501.

60 J. Gibson, A. P. Monkman and T. J. Penfold, The Importance of Vibronic Coupling for Efficient Reverse Intersystem Crossing in Thermally Activated Delayed Fluorescence Molecules, *ChemPhysChem*, 2016, **17**, 2956–2961.

61 M. K. Etherington, J. Gibson, H. F. Higginbotham, T. J. Penfold and A. P. Monkman, Revealing the spin–vibronic coupling mechanism of thermally activated delayed fluorescence, *Nat. Commun.*, 2016, **7**, 13680.

62 M. K. Itokazu, A. S. Polo and N. Y. M. Iha, Luminescent rigidochromism of fac-[Re(CO)3(phen) (cis-bpe)]+ and its binuclear complex as photosensors, *J. Photochem. Photobiol., A*, 2003, **160**, 27–32.

63 J. M. Younker and K. D. Dobbs, Correlating Experimental Photophysical Properties of Iridium(III) Complexes to Spin–Orbit Coupled TDDFT Predictions, *J. Phys. Chem. C*, 2013, **117**, 25714–25723.

64 J. Yan, Z. H. Qu, D. Y. Zhou, S. M. Yiu, Y. Qin, X. Zhou, L. S. Liao and Y. Chi, Bis-tridentate Ir(III) Phosphors and Blue Hyperphosphorescence with Suppressed Efficiency Roll-Off at High Brightness, *ACS Appl. Mater. Interfaces*, 2024, **16**, 3809–3818.

65 H. Nakanotani, T. Higuchi, T. Furukawa, K. Masui, K. Morimoto, M. Numata, H. Tanaka, Y. Sagara, T. Yasuda and C. Adachi, High-efficiency organic light-emitting diodes with fluorescent emitters, *Nat. Commun.*, 2014, **5**, 4016.